JGR Solid Earth

RESEARCH ARTICLE

10.1029/2020JB020834

Key Points:

- We present 13 new $^{40}Ar/^{39}Ar$ age determinations from the Erebus Volcanic Province, Antarctica (−78°, 167°)
- We present 98 high-quality site directions resulting in virtual geomagnetic pole scatter consistent with model predictions and a paleopole consistent with GAD
- We present 26 new paleointensities that yield an estimated average dipole moment of 44 ± 3.6 ZAm^2

Supporting Information:

- Supporting Information S1
- Table S2

Correspondence to:

H. Asefaw,
hasafaw@ucsd.edu

Citation:

Asefaw, H., Tauxe, L., Koppers, A. A. P., & Staudigel, H. (2021). Four-Dimensional paleomagnetic dataset: Plio-Pleistocene paleodirection and paleointensity results from the Erebus Volcanic Province, Antarctica. *Journal of Geophysical Research: Solid Earth*, *126*, e2020JB020834. https://doi.org/10.1029/2020JB020834

Received 25 AUG 2020
Accepted 25 NOV 2020

Four-Dimensional Paleomagnetic Dataset: Plio-Pleistocene Paleodirection and Paleointensity Results From the Erebus Volcanic Province, Antarctica

H. Asefaw[1], **L. Tauxe**[1], **A. A. P. Koppers**[2], **and H. Staudigel**[1]

[1]Geosciences Research Division, Scripps Institution of Oceanography, University of California San Diego, La Jolla, CA, USA, [2]College of Earth, Ocean and Atmospheric Sciences, Oregon State University, Corvallis, OR, USA

Abstract A fundamental assumption in paleomagnetism is that a geocentric axial dipole (GAD) geomagnetic field structure extends to the ancient field. Global paleodirectional compilations that span 0–5-million year support a GAD dominated field structure with minor non-GAD contributions, however, the paleointensity data over the same period do not. In a GAD field, higher latitudes should preserve higher intensity, but the current database suggests that intensities are independent of latitude. To determine whether the seemingly “low” intensities from Antarctica reflect the ancient field, rather than low-quality data or inadequate temporal sampling, we have conducted a new study of the paleomagnetic field in Antarctica. This study focuses on the paleomagnetic field structure over the Plio-Pleistocene. We combine and reanalyze new and published paleodirectional and paleointensity results from the Erebus volcanic province to recover paleodirections from 98 sites that were both thermally and alternating field demagnetized and then subjected to a set of strict selection criteria and paleointensities from 26 sites from the Plio-Pleistocene that underwent the IZZI modified Thellier-Thellier experiment and were also subjected to a strict set of selection criteria. The paleopole (201.85°, 87.65°) and α_{95} (5.51°) recovered from our paleodirectional study supports the GAD hypothesis and the scatter of the virtual geomagnetic poles falls within the uncertainty of that predicted by TK03 paleosecular variation model. Our time-averaged field strength estimate, 33.57 ± 2.71 μT, is significantly weaker than that expected from a GAD field estimated by the present field.

Plain Language Summary The geocentric axial dipole (GAD) hypothesis states that the Earth's magnetic field may be approximated by an Earth-centric dipole aligned with the rotation axis. This hypothesis is fundamental for paleogeographic reconstructions of the tectonic plates. While global paleomagnetic directions from the last 5 million years recover a predominately GAD field structure, paleointensity estimates over the same time period do not. In this study, we re-examine the paleomagnetic field structure in the Erebus Volcanic Province, Antarctica, and recover a robust data set of directional and intensity data. We then compare the paleopole and average dipole moment against a GAD field structure and model predictions of paleosecular variation.

1. Introduction

A geocentric axial dipole (GAD) field is the magnetic field generated by a dipole that is positioned in the center of the Earth and aligned along the spin axis (Gilbert, 1958). In mathematical representations of the geomagnetic field structure, such as the International Geomagnetic Reference Field (IGRF), the axial dipole term (g_1^0) accounts for the majority of the field (Lowes, 1973). However, modern geomagnetic field strengths around the globe (Figure 1a) also reveal latitudinal and longitudinal non-GAD features and regions with anomalously low (e.g., the South Atlantic Anomaly) and high intensities. It is frequently assumed (e.g., McElhinny, 2007) that the field, when averaged over sufficient time, is well approximated by a GAD field. Given a GAD field (Figure 1b) both the intensity of the geomagnetic field (B) and the inclination (I) would vary with latitude (λ) by:

$$B = M\sqrt{1 + 3\cos^2(\frac{\pi}{2} - \lambda)} \tag{1}$$

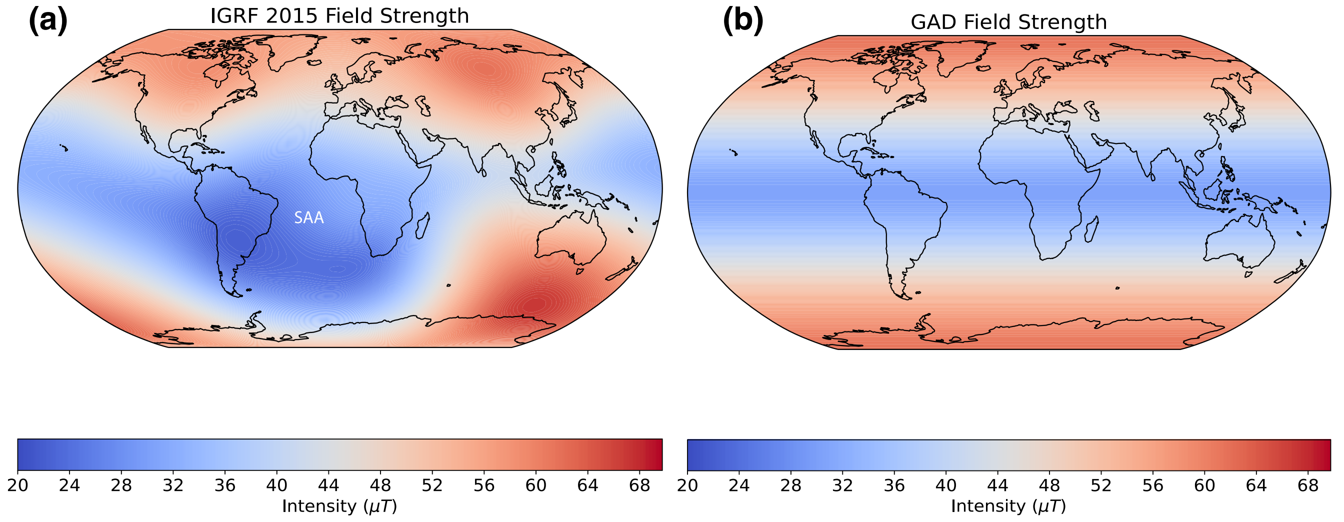

Figure 1. (a) Intensity of the geomagnetic field estimated from the 2015 IGRF model. (b) Intensity of the geomagnetic field expected for a GAD field with an 80 ZAm^2 magnetic moment. GAD, geocentric axial dipole; IGRF, International Geomagnetic Reference Field.

and

$$\tan(I) = 2\tan(\lambda) \tag{2}$$

where M is the g_1^0 term in nT.

Both the GAD and non-GAD terms of the geomagnetic field vary with time, a phenomenon known as secular variation. The terms of the IGRF have been estimated for the last century or so (Thébault et al., 2015), using geomagnetic observatory and, more recently, satellite data. From 1600 to modern, IGRF-like models were based on ship-board measurement data (Jackson et al., 2000) data from geomagnetic observatories. Prior to about 1600, measurements of the geomagnetic field are too scare for constraining reference models and so we rely on geological and archeological materials (e.g., Constable et al., 2016). The paleomagnetic field structure can be preserved in the geological record and various techniques allow us to the recover paleodirections (Creer, 1967; Irving et al., 1961; Stephenson, 1967) and paleointensities (Coe, 1967; Hoffman & Biggin, 2005; Shaw, 1974; Thellier & Thellier, 1959; Walton & Shaw, 1992; Yu et al., 2004). Independent studies of the paleofield are then compiled into paleomagnetic databases (e.g., the MagIC database at: earthref.org/MagIC). We can then use these data to characterize paleosecular variation (PSV) and the time-averaged field (TAF). Changes in the structure of the geomagnetic field at the surface of the Earth reflect the dynamics occurring in the fluid outer core (Glatzmaier & Coe, 2007; Holme, 2007; Jackson & Finlay, 2007; Livermore et al., 2014) so an accurate characterization of the field is important for understanding the outer core.

Numerous studies (Behar et al., 2019; Johnson et al., 2008; Opdyke & Henry, 1969; McElhinny & Lock, 1996) have recovered paleodirections from the last 5 million years that are largely consistent with a GAD field with minor non-GAD terms. Early compilations of absolute paleointensities were also interpreted as largely consistent with a GAD structure (McFadden & McElhinny, 1982; Tanaka et al., 1995) from a paleomagnetic dipole moment (PDM) similar to the present dipole moment, ~80 ZAm^2. Selkin and Tauxe (2000) examined data from submarine basaltic glass over the last 5 million years and found a reasonable fit to intensities predicted by a PDM of ~45 ZAm^2. However, the dipole signature over the last 5 million years is not evident in modern absolute paleointensity databases (Figure 2), which include data from a variety of materials and methods (e.g., PINT15 of Biggin, 2010 and the MagIC database at https://earthref.org/MagIC). The lack of a dipole signal in the current global database may reflect a paleomagnetic field structure with stronger non-GAD components than previously recognized or a bias in the global dataset as a consequence of poor temporal sampling, poor experimental design or poor choice of sample materials. Therefore, the reliability of the data is key to understanding the behavior of the geomagnetic field.

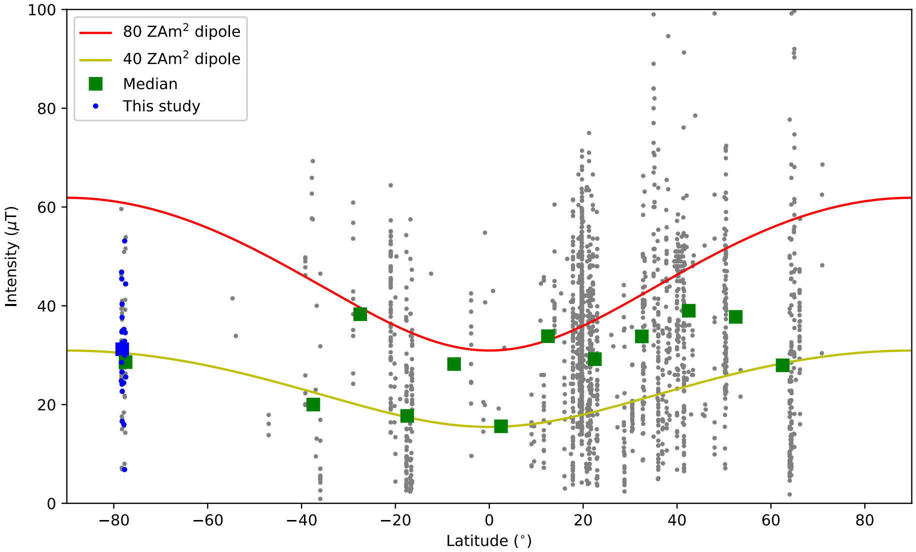

Figure 2. Global paleointensity estimates over the last 5 million years (gray circles) taken from the PINT15 database (Biggin, 2010) of absolute paleointensities. The intensity estimates are binned into 10° latitude intervals. The median value of bins with 10 or more sites is plotted as green squares. The results from this study are marked as blue points along with their median intensity (blue square). The yellow curve (red curve) marks the intensity at a given latitude expected for a dipole moment of 40 ZAm^2 (80 ZAm^2).

Recovering paleointensity is challenging owing to the complex magnetization acquisition behavior of nonideal magnetic grains (Dunlop & Özdemir, 2001; Dunlop et al., 2005; Tauxe & Yamazaki, 2015) and the tendency for magnetomineralogical alteration during paleointensity experiments (Coe, 1967; Smirnov & Tarduno, 2003). To determine whether the "low" intensities measured at the high southerly latitudes are an artifact of nonideal magnetic recorders or are in fact an accurate representation of the paleomagnetic field, we conducted an extensive study of the paleomagnetic field in the Erebus Volcanic Province, Antarctica (−78°, 167°). We targeted the finest grained (glassiest) rock samples (Cromwell et al., 2015; Selkin & Tauxe, 2000), treated them to a rigorous experimental protocol (Yu et al., 2004) and subjected the results to a set of strict selection criteria (Cromwell et al., 2015). In this study, we present a robust four-dimensional paleomagnetic data set from the Erebus Volcanic Province, Antarctica that includes 98 paleodirections to characterize PSV and 26 paleointensities to recover the TAF over the Plio-Pleistocene.

2. Methods

2.1. Sample Collection

Mankinen and Cox (1988) drilled between six and eight oriented core samples from the interior of lava flows around the Erebus Volcanic Province, Antarctica (Figure 3) and reported directions from the natural remanent magnetization (NRM). Tauxe et al. (2004) analyzed the Mankinen/Cox sample collection for directions and intensities. Lawrence et al. (2009) reported on a larger suite of samples collected in two field seasons (2003/2004 and 2005/2006), which included at least 10 cores per lava flow; they compiled all the paleodirectional and paleointensity experiments from these cores and those collected earlier by Mankinen and Cox (1988).

Several recent studies (e.g., Cromwell et al., 2015) have suggested that finer grained lava flow tops, as opposed to flow interiors, coupled with the use of stricter selection criteria, may result in more accurate and precise estimates of paleointensity. We, therefore, applied the selection criteria proposed by Cromwell et al. (2015), here called CCRIT, to reanalyze the paleointensity results of Lawrence et al. (2009). In our reanalysis, only a dozen of the original 41 sites that passed the criteria used by Lawrence et al. (2009) pass the CCRIT criteria. Therefore, in the 2015/2016 Antarctic field season, we resampled 141 of the original sites reported by Lawrence et al. (2009) for this study. We targeted the surfaces of each lava flow. Where possible, we identified the original sites (Table 3) using the 1-in. drill holes remaining in the outcrop. The

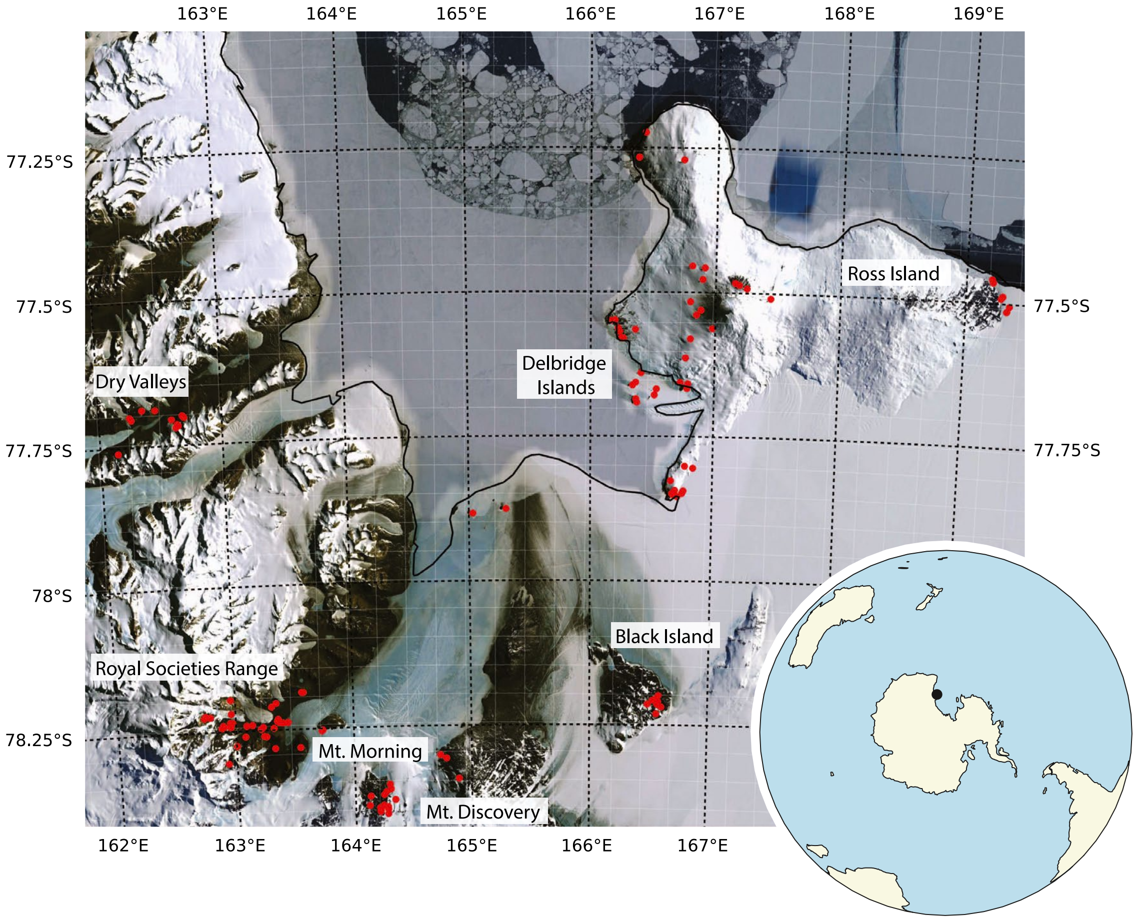

Figure 3. A natural color satellite image of the Erebus Volcanic Province, Antarctica. Our sites (red circles) include the Dry Valleys, Royal Societies Range, Mt. Morning, Mt. Discovery, Black Island, and Ross Island.

remainder were located by GPS coordinates from Lawrence et al. (2009) and approximated from the maps and descriptions in Mankinen and Cox (1988). Once we identified the original sampling sites, we resampled the microcrystalline, glassy material from the lava flow top or flow bottom. We collected hand samples using hammers and chisels. The outcrops included lava flows, pillow lavas, and hyaloclastite cones that formed over the Plio-Pleistocene. Several lava flows from the original study yielded identical directions and re-examination in the field confirmed that these sites sampled the same lava flow. In this study, we combine duplicate sites into a single site (see Table S1).

2.2. Paleointensity

2.2.1. Recovering Paleointensity

Magnetic grains in igneous rocks acquire a thermal remanent magnetization (TRM) by cooling from temperatures well above their Curie temperature through their blocking temperatures (T_b). Once the grain cools below T_b, the resulting TRM captures an instantaneous record of the geomagnetic field that can remain stable over long timescales. The degree of alignment between the magnetic grain moments and the ambient field depends on the strength of the field (B) at the time of cooling (Néel, 1955). For a given population of magnetic grains,

$$M_{TRM} = M_s \tanh \frac{vM_s(T_b)B}{kT_b}, \tag{3}$$

where M_{TRM} is the net magnetization, k is the Boltzmann constant, v is magnetic grain volume, and $M_s(T_b)$ is spontaneous magnetization at T_b.

In a weak magnetic field (of the order of the modern geomagnetic field), TRM acquisition is generally assumed to be quasilinearly proportional to the strength of the ambient field. This proportionality allows us to recover the intensity of the geomagnetic field when the rock formed. The NRM may be removed by heating the rock and cooling it in zero external field. A new TRM overwrites the NRM by cooling the rock in a controlled field in the laboratory. The TRM acquired in the applied field is proportional to the NRM acquired in the paleomagnetic field (Néel, 1955). Thus, we can estimate the intensity of the paleomagnetic field by

$$B_{anc} = \frac{M_{NRM}}{M_{TRM}} B_{lab}, \tag{4}$$

where M_{NRM} is the natural remanent magnetization, B_{lab} is the field applied in the lab, M_{TRM} is the thermal remanent magnetization imparted by heating the specimen, then cooling it in the lab field, and B_{anc} is the strength of the paleomagnetic field. A rock contains an assemblage of magnetic grains and each grain blocks its magnetization at a different temperature. Therefore, incrementally demagnetizing and remagnetizing a rock sample at progressively higher temperatures results in several independent estimates of the paleofield, assuming independence of partial TRMs (pTRM) acquired and lost in different temperature intervals.

2.2.2. Specimen Preparation

Samples were crushed into 100–500-mg fragments. The fragments were then examined under a binocular microscope to select the individual specimens that appeared the finest grained and least altered. These glassy (or microcrystalline) specimens may contain the single domain (SD) grains of magnetite that follow Thellier's laws (Thellier, 1938) and allow us to recover an accurate paleointensity estimate. Each individual specimen was swaddled in glass microfiber filter paper and affixed inside a borosilicate glass vial with K_2SiO_3. The specimens were then placed in a transformer steel shielded room in the Paleomagnetic Laboratory at Scripps Institution of Oceanography for the duration of the experiment.

2.2.3. IZZI Modified Thellier-Thellier Experiment

We conducted the IZZI-modified Thellier-Thellier protocol (Tauxe & Staudigel, 2004; Yu et al., 2004), whereby specimens are incrementally heated and cooled either in the absence of a magnetic field to demagnetize the NRM (a zero-field step) or in the presence of an applied lab field to impart a pTRM (an in-field step). Specimens were subjected to both an in-field (I) and zero-field (Z) treatment at each temperature step. Temperature steps were conducted at 100°C intervals from 0°C to 400°C, then 25°C intervals up to 500°C, and finally at 10°C intervals until each specimen was completely demagnetized. Specimens were heated in custom-built furnaces in the Scripps Paleomagnetic Laboratory; these furnaces have thermocouples in noninductively wound heating elements to control the temperature to within a few degrees with reproducibility of better than one degree. Specimens were rapidly air-cooled following treatment. During in-field treatment steps, specimens were cooled in a 30 μT field. The order of the treatment, IZ (Aitken et al., 1988) or ZI (Coe, 1967), alternated with each temperature step in order to detect tails (pTRMs imparted at a given temperature that were not removed by treatment in zero field at the same temperature), and zero-field memory effects (Aitken et al., 1988) in the ZI sequence. We applied pTRM checks, additional in-field treatments at a previously measured temperature step, between the ZI and the IZ sequences in order to monitor mineral neoformation and magnetomineral alteration (Coe, 1967). Immediately following treatment, we measured the magnetic remanence with a 2G Cryogenic SQUID (superconducting quantum interference device) magnetometer in the Scripps Paleomagnetic Laboratory.

We conducted a preliminary IZZI-modified Thellier-Thellier experiment (Tauxe & Staudigel, 2004; Yu et al., 2004) on 144 specimens from 99 samples, with, 1 to 2 specimens from each sample. The results from this preliminary experiment allowed us to target our efforts to the most promising sites from which we selected up to six additional specimens. In total, we measured 381 specimens.

2.2.4. Cooling Rate

The TRM acquired by each specimen is affected by its rate of cooling (Dodson & McClelland-Brown, 1980; Fox & Aitken, 1980; Halgedahl & Fuller, 1980; Santos & Tauxe, 2019). After each treatment, specimens were rapidly air-cooled to match the rate at which we suspect they initially cooled. We compare the impact of cooling rate on TRM acquisition in our specimens to that in the specimens studied by Lawrence et al. (2009) from the, presumably, slower cooled lava flow interiors. We conducted a cooling rate experiment whereby we heated the specimens to 620° in a 50 μT field, cooled them in under an hour, and then measured their TRM. We then reheated the specimens to 620° in a 50 μT field and allowed them to cool without a fan for approximately 12 h, and remeasured the resulting TRM. The ratio of the two measurements allows us to assess the effect of cooling rate on the TRM.

2.2.5. Nonlinear TRM Acquisition

The Thellier method (Thellier & Thellier, 1959) assumes that the magnetic carriers are SD noninteracting grains of magnetite that acquire a TRM in proportion to the ambient field in low magnetic fields, yet several studies have detected nonlinear TRM acquisition (e.g., Ben-Yosef et al., 2009; Selkin et al., 2007). Therefore, after we completed the IZZI experiment, we selected specimens from sites that met the CCRIT criteria in both our and Lawrence et al. (2009)'s experiments. We then performed an additional set of steps to detect nonlinear TRM acquisition behavior. We subjected these specimens to a total TRM by cooling from 630°C, in treatment fields of 0, 15, 20, 30, 40, 50, and 60 μT.

2.3. Paleodirection

2.3.1. Alternating Field Demagnetization and Thermal Demagnetization

Lawrence et al. (2009) recovered paleodirections by stepwise thermal demagnetization or alternating field (AF) demagnetization. Each oriented drill core was cut into 1-in. specimens, at least five of which were subjected to either AF or thermal demagnetization. A total of 461 specimens were AF demagnetized in a Sapphire Instruments SI-4 uniaxial AF demagnetizer in the Scripps laboratory. Specimens were treated in 5 mT steps from 5 to 20 mT, 10 mT steps from 20 to 100 mT, and then at 120, 150, and 180 mT or until the NRM was removed. An additional 323 specimens were thermally demagnetized by stepwise heating in 50°C intervals from 0°C to 500°C, in 25°C intervals from 520°C to 560°C and in 5°C to 10°C intervals until the specimens were entirely demagnetized. After each treatment, we measured the remaining NRM. The demagnetization path, as represented by Zijderveld diagrams (Zijderveld, 1967) monitors the stability and behavior of the magnetization vector as the specimen is demagnetized. For this study, we thermally demagnetized an additional 44 specimens to increase the number of paleodirectional estimates per site from 5 to 6 following the suggestion of Behar et al. (2019) who found decreased scatter and increased consistency with GAD by using more specimens per site and stricter within-site scatter criteria.

2.4. Hysteresis and FORCs

Lawrence et al. (2009) describe paleointensity experiments conducted on specimens that were drilled from the interior of the lava flows and collected by Mankinen and Cox (1988) and analyzed by Tauxe et al. (2004). Here we report on new experiments conducted on samples that were hand collected from the surface or base of the lava flow. As described in the following, six sites had specimens with successful intensity estimates from samples collected from both the interior (presumably coarser grained) and the flow top. We selected sister specimens from these sites and measured hysteresis loops and FORC diagrams (Pike et al., 1999; Roberts et al., 2000) with a Princeton Measurements Corporation Micromag Alternating Gradient Magnetometer in an attempt to diagnose domain state. We plotted the results using the FORCinel software package (Harrison & Feinberg, 2008). We applied a smoothing factor of 1 and removed first-point artifacts.

2.5. ^{40}Ar/^{39}Ar Geochronology

Eighteen samples were selected for ^{40}Ar/^{39}Ar age dating. All Ar-Ar age analyses were conducted at the Argon Geochronology Lab at Oregon State University following the procedure of Koppers et al. (2008). A 200–300 μm groundmass specimen was selected from each sample then leached in an ultrasonic bath with (1 and 6N) HCl and (1 and 3N) HNO_3^- and rinsed with distilled water to remove any alteration products. Once cleaned, samples were irradiated in the TRIGA CLICIT nuclear reactor at OSU to convert ^{39}K to ^{39}Ar. The irradiated samples were then incrementally heated in 21–44 temperature steps for 5–7 min each with a defocused CO_2 laser beam that scanned the sample to release the argon. Argon isotopes were measured by an ARGUS-VI multicollector mass spectrometer.

The age of the sample is estimated by plateau and inverse isochron ages to ensure the two estimates are concordant at the 95% confidence level. To estimate the plateau age, an age and uncertainty is first calculated for each temperature step by using the measured ratio of ^{40}Ar to ^{39}Ar. A plateau is then selected from this age spectrum that includes at least three incremental heating steps with overlapping 2σ confidence levels and at least 50% of the total $^{39}Ar_k$ released. The plateau age of the sample is estimated from the mean plateau age and its reliability by the mean square weighted deviate. To determine the inverse isochron age, the ratio of ^{36}Ar/^{40}Ar is plotted against ^{39}Ar/^{40}Ar. A regression line is selected that includes at least five heating steps and each data point to within 3σ of the ^{39}Ar/^{40}Ar and ^{36}Ar/^{40}Ar weighted means (Heaton & Koppers, 2019). The inverse isochron age is calculated from the intercept value of ^{39}Ar/^{40}Ar; the initial ^{40}Ar/^{36}Ar in the sample is calculated from the y-intercept and serves to verify the assumed trapped argon signature in the sample assumed in the plateau age calculations.

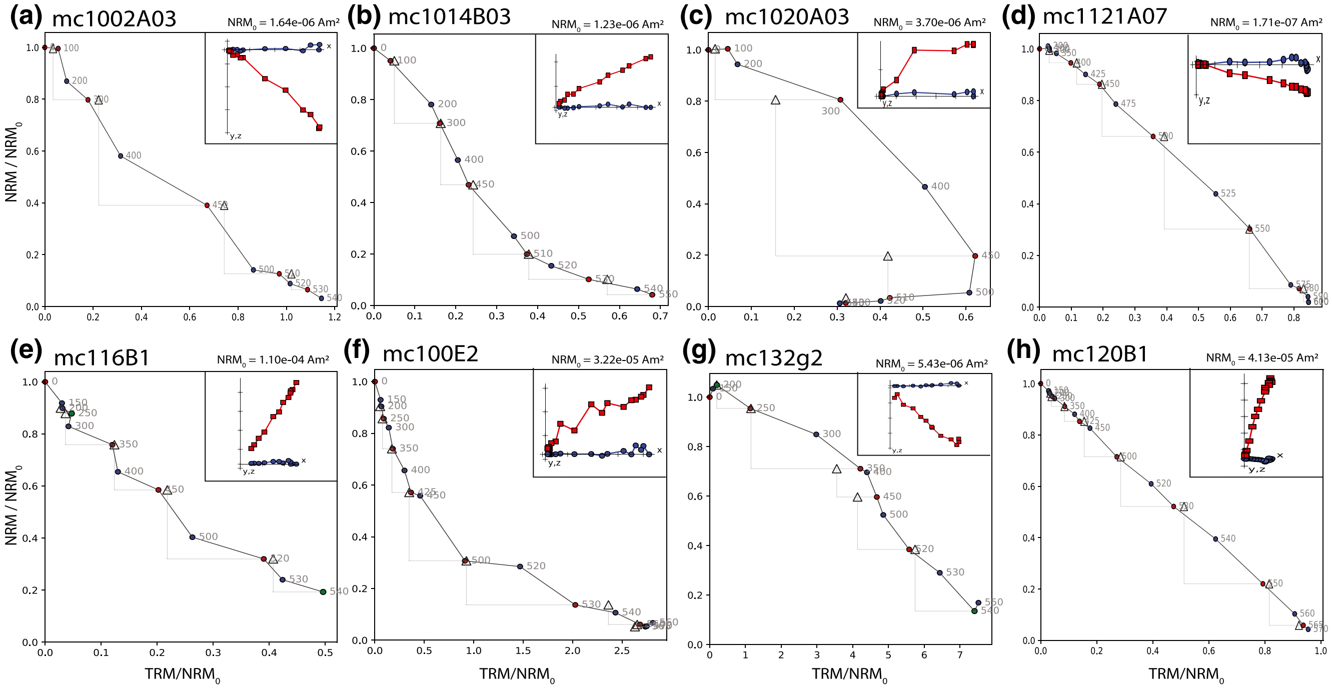

Figure 4. Representative Arai diagrams and Zijderveld diagrams (insets) of the different behaviors observed in our unoriented specimens. White triangles mark pTRM checks. Red (blue) circles indicate an in-field treatment preceded a zero-field treatment (zero-field treatment preceded an infield treatment) at the corresponding temperature. (a)–(d) are results from this study and (e) and (f) from (Lawrence et al., 2009). (a, e) zig-zagging; (b, f) nonlinearity and sagging; (c, g) failed pTRM checks; (d, h) "well-behaved" specimens where the proportion of NRM remaining to pTRM acquired is identical between each set of temperature steps. NRM, natural remanent magnetization; pTRM, partial TRM; TRM, thermal remanent magnetization.

Table 1

Selection Criteria (Paterson et al., 2014) Applied to the Data From the IZZI-Modified Thellier-Thellier Experiment

n	DANG	MAD	β	SCAT	Frac	$G_{\max}$	$\lvert \vec{k} \rvert$	N	$B_{\%}$	$B\sigma$
4	≤5°	≤5°	0.1	TRUE	0.78	≤0.6	0.164	3	10	4 μT

Note. n, minimum number of consecutive demagnetization steps; DANG, deviation angle; MAD, maximum angle of deviation; β = the maximum ratio of the standard error to the best fit slope; SCAT, a Boolean value that indicates whether the data fall within $2\sigma_{\text{threshold}}$ of the best fit slope; FRAC, fractional remanence, $G_{\max}$, maximum fractional remanence removed between consecutive temperature steps; $\vec{k}$, maximum curvature statistic (1/radius of the best-fitting circle), N, minimum number of specimens per sample; $B_{\%}$, maximum percentage standard deviation from the site average intensity; B_{σ}, maximum intensity (μT) deviation from the site average intensity.

3. Results

3.1. Paleointensity

We present representative results of our IZZI experiment as Arai diagrams (Nagata et al., 1963) in Figure 4, in order to compare the ratio between NRM remaining to pTRM acquired for each pair of temperature steps and to monitor any changes in this ratio. We present the magnetization directions as Zijderveld diagrams (Zijderveld, 1967) in the insets in Figure 4. Despite our best effort to collect microcrystalline material, our specimens often did not behave as the noninteracting uniaxial SD grains of magnetite assumed by Néel theory (Néel, 1955) and required by Thellier's laws (Thellier & Thellier, 1959). Instead, many specimens exhibit nonideal behavior (i.e., zig-zagging or nonlinear Arai plots, failed pTRM checks, or multiple components of magnetization) resulting in potentially unreliable paleointensity estimates.

3.1.1. Nonideal Behavior: Nonlinear Arai Plots

Nonlinear behavior appears as zig-zagging and sagging in the Arai plots. Zig-zagging in the Arai diagram Figures (4a and 4e) occurs when the ratio of NRM remaining to pTRM acquired varies between different temperature intervals based on the sequence of treatment steps (IZ or ZI). During the IZZI modified Thellier-Thellier experiment, the order in which the treatments are applied, in-field then zero-field or zero-field then in-field, alternates at each temperature step (Yu et al., 2004). The alternating sequence is used to detect so-called "pTRM tails" (Shashkanov & Metallova, 1972), in particular, high-temperature tails, as well as zero-field memory effects (Aitken et al., 1988). High temperature tails occur either when the pTRM acquired by heating to temperature T in a field is not entirely removed when the specimen is reheated to the same temperature and cooled in a zero-field. Sagging Arai plots (see e.g., Figures 4b and 4f) may result from displaced blocking and unblocking temperature spectra in which the blocking temperatures are higher than the unblocking temperatures (Dunlop & Özdemir, 2001). Both zig-zagging and sagging likely result

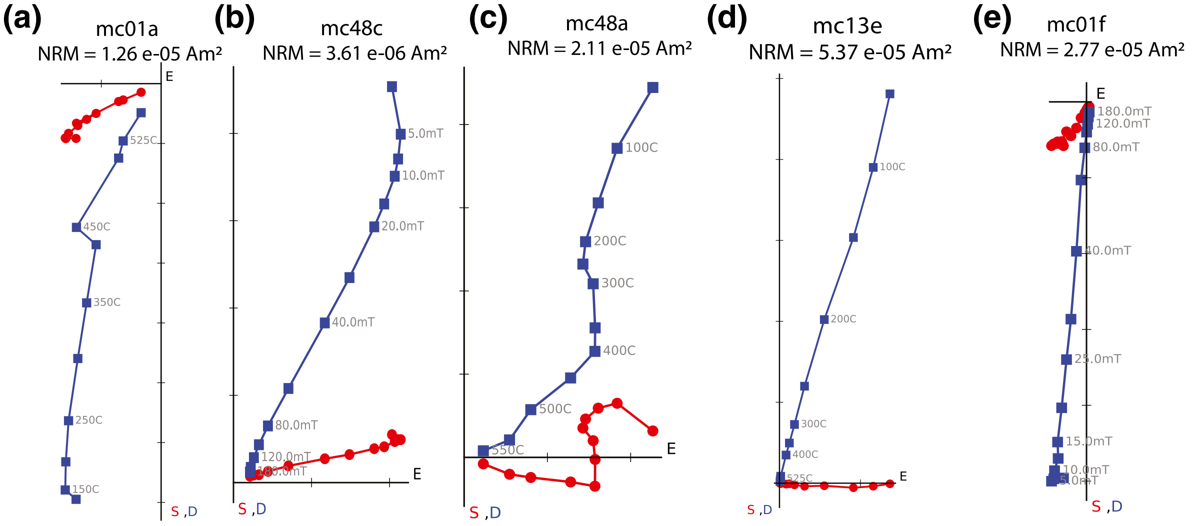

Figure 5. Representative Zijderveld diagrams of the directional behaviors observed in our specimens. The projection of the demagnetization vector onto the vertical plane is marked in blue and the projection of the same vector onto the horizontal plane is marked in red. (a) Two reverse polarity directions with distinct blocking temperature spectra. A low-temperature direction is removed 0–400° and a higher temperature component demagnetizes between 450° and 600°. (b) Two normal polarity directions with distinct coercivity spectra. The low-coercivity component is removed between 0 and 10 mT. (c) An unstable normal polarity direction from a thermal demagnetization experiment. The specimen may include several directions with overlapping blocking temperature spectra. (d) A single stable normal polarity direction from a thermal demagnetization experiment (e) A single stable reverse polarity direction from an AF demagnetization experiment. AF, alternating field.

Table 2
Selection Criteria Applied to Our Directional Data

MAD	DANG	*N*	*k*
≤5°	≤5°	≥6	≥100

DANG, deviation angle; *k*, precision parameter; MAD, maximum angle of deviation; *N*, minimum cores per site.

from the presence of non-SD grains (e.g., Dunlop & Özdemir, 2001; Krása et al., 2003).

3.1.2. Nonideal Behavior: Failed pTRM Checks

A pTRM check (Coe, 1967) is a previously measured in-field treatment that is repeated. Here we insert a pTRM check after every ZI-IZ pair (Coe, 1967; Tauxe & Staudigel, 2004). Any deviation in the remanence (triangles in Figures 4c and 4g) indicates magnetomineral alteration.

3.1.3. Ideal Behavior and Selection Criteria

To filter out the specimens that exhibited nonideal behavior (Figure 4), we applied a set of selection criteria at the specimen and site level. A wide range of selection criteria (Kissel & Laj, 2004; Leonhardt et al., 2004; Selkin & Tauxe, 2000; Tauxe et al., 2016) and paleointensity statistics (Paterson et al., 2014) exists to separate low- and high-quality paleointensity data. We modeled our criteria (Table 1) after those of (Cromwell et al., 2015), in which they successfully recovered accurate and precise estimates of paleointensity of historical Hawaiian lava flows. This set is referred to as the "CCRIT" set of paleointensity criteria (Tauxe et al., 2016).

Table 3
Successful Paleointensity Results From This Study

Site	Lat (°)	Lon (°)	VADM (ZAm^2)	*n*	Int. (μT)	Age (Ma)
mc1004	−77.84	166.69	46.33 ± 0.31	3	35.23	0.34 ± 0.01
mc1015	−77.46	169.21	33.66 ± 0.94	3	25.57	1.33 ± 0.02
mc1019	−77.88	165.30	32.08 ± 0.2	3	24.40	0.0811 ± 0.0151
mc1029	−78.31	164.79	59.7 ± 0.5	7	45.46	0.18 ± 0.08
mc1030	−78.34	164.88	61.49 ± 2.75	4	46.82	
mc1031	−78.35	164.30	40.27 ± 0.99	3	30.67	0.133 ± 0.0117
mc1032	−78.35	164.30	37.46 ± 0.24	4	28.52	0.0078 ± 0.012
mc1035	−78.39	164.24	32.52 ± 0.43	3	24.77	0.12 ± 0.02
mc1109	−78.28	163.54	42.69 ± 1.75	3	32.50	1.26 ± 0.04
mc1115	−78.24	162.96	41.04 ± 2.12	5	31.24	2.46 ± 0.31
mc1117	−78.24	162.97	34.98 ± 0.13	4	26.62	2.28 ± 0.24
mc1119	−78.24	162.96	49.49 ± 1.21	4	37.67	1.08 ± 0.22
mc1120	−78.24	163.09	31.7 ± 0.19	3	24.13	1.76 ± 0.05
mc1121	−78.23	162.95	53.0 ± 2.53	6	40.35	2.51 ± 0.06
mc1128	−78.21	166.57	45.85 ± 1.07	3	34.90	8.75 ± 0.03
mc1131	−78.21	166.57	21.81 ± 0.32	5	16.60	9.66 ± 0.18
mc1139	−78.26	163.08	40.94 ± 0.99	3	31.17	0.88 ± 0.08
mc1140	−78.28	163.00	45.58 ± 3.51	3	34.70	2.03 ± 0.09
mc1142	−77.85	166.68	20.98 ± 2.57	4	15.95	1.23 ± 0.02
mc1147	−78.20	162.96	29.78 ± 2.06	3	22.67	1.63 ± 0.34
mc1155	−77.70	162.25	39.42 ± 0.16	3	29.97	1.5 ± 0.05
mc1157	−77.70	162.26	43.18 ± 1.54	4	32.83	1.71 ± 0.01
mc1164	−77.51	169.33	107.63 ± 2.51	3	81.77	1.36 ± 0.01
mc1167	−77.49	169.29	58.49 ± 0.12	3	44.43	
mc1207	−77.68	166.52	69.91 ± 0.42	3	53.13	0.5187 ± 0.0043
mc1217	−77.51	167.44	40.7 ± 2.91	5	30.92	0.16 ± 0.01
mc1218	−77.56	166.98	45.48 ± 1.23	5	34.56	0.03 ± 0.01
mc1306	−77.70	162.69	9.0 ± 0.03	3	6.84	2.56 ± 0.13

Note. We include the results from two sites, mc1128 and mc1131, that passed our set of selection criteria but exceeded the age bounds of this study. VADM, virtual axial dipole moment (ZAm^2); Int, paleointensity (μT); *n*, samples.

CCRIT applies two directional statistics, Deviation ANGle (α of Selkin & Tauxe, 2000; *dev* of Tanaka & Kobayashi, 2003; and DANG in Paterson et al., 2014) and the maximum angle of deviation (MAD; Kirschvink, 1980) to determine the variability in the direction of the NRM. MAD quantifies the amount of scatter in the directions while DANG calculates the angle between the best-fit line for the demagnetization direction and the origin. Three additional parameters are SCAT and FRAC of Shaar and Tauxe (2013), and $|\vec{k}|$ of Paterson (2011) applied over interval used (k') of Cromwell et al. (2015); these are applied to test the assumption of linearity of the Arai plot. SCAT constrains the amount of scatter permitted between the best fit proportionality constant and the demagnetization data and pTRM checks; FRAC ensures the majority of the remanence is used to calculate paleointensity; $\vec{k}$ quantifies the amount of curvature. CCRIT also tests for consistency between estimates at the site level by setting thresholds on the percent error ($\beta_{\%}$) and standard deviation (β_{σ}) permitted for specimen at a site. Of original 135 sites, 26 passed these selection criteria and fall within the Plio-Pleistocene (Table 3). These 26 sites yield a 33.57 ± 2.71 μT average intensity or equivalently a paleomagnetic axial dipole moment (PADM) of 44.13 ± 3.57 ZAm^2.

3.2. Paleodirection

We determined the best fitting direction through the vectors of each oriented specimen using principal component analysis (Kirschvink, 1980). The results of the demagnetization experiments vary from multiple unstable directions (e.g., Figures 5a–5c) to a single stable direction (e.g., Figures 5d and 5e). Multiple directions with distinct coercivity and blocking temperature spectra decay along one direction at low field and temperature treatments then abruptly shift to decay along a different direction for the final, characteristic, remanent magnetization (ChRM; Figure 5a and 5b). The low-temperature or low-coercivity component may result from a viscous remanent magnetization or a partial overprint that is typically removed after the first or second treatment step. Multiple components with overlapping blocking temperature spectra appear as zig-zagging or gradual shifts in the demagnetization curve (Figure 5c). Zig-zagging may result from pTRM tails, if the thermal demagnetization data was derived from an IZZI experiment. We also observe gradual changes in the magnetization direction where there may be multiple directional components that are removed in different proportions between each treatment step. We applied a set of criteria (Table 2) to select the final stable component of the demagnetization vector, the ChRM. At the specimen level, at least four demagnetization steps were used to determine the ChRM and MAD and DANG were set to 5° to constrain the direction. Lawrence et al. (2009) used site level thresholds of $N > 4$ and $\kappa > 50$ as acceptance criteria. Following Behar et al. (2019), we required at least six samples per site (N) that pass our criteria. We then calculate the site average direction and set the minimum threshold for κ (Fisher, 1953), a precision parameter to quantify the dispersion in the directions, to 100. Ninety-eight sites yield reliable paleodirections (Table 4). The 98 Plio-Pleistocene directions resulted in a paleopole that is consistent with the spin axis (201.9°, 87.7°, and α_{95} 5.5°).

3.3. Hysteresis and FORCs

Several sites (mc1030, mc1032, mc1115, mc11121, mc1147, and mc1157) passed CCRIT and included estimates from samples that were collected from both the interior (Lawrence et al., 2009) and surface of the same lava flow (this study). At sites mc1030, mc1115, mc1147, and mc1157, the estimates from the interior are 2–8 μT lower than the paleointensity estimates from the lava flow tops (Figure 6). We selected sister specimen for hysteresis loops and FORCs (Harrison & Feinberg, 2008) to examine the domain state or magnetic interactions that may explain the difference.

Although each sister specimen passed CCRIT, the specimens exhibit a mixture of magnetic components in the FORCs. We interpret the horizontal ridge in the FORC diagram near $B_u = 0$ mT (Figure 7) as the contribution from SD grains after Roberts et al. (2000) and Pike et al. (2001). The distribution of coercivities (B_c) ranges from 0 to 50 mT and peaks between 0 and 10 mT in our surface specimen and 10–20 mT in our interior specimen. This peak is offset from the $B_u = 0$ mT axis. The contours are shifted downward from this ridge, which reflects the level of interaction fields between the SD grains. Specimen mc115a2 (Figure 7b) displays superparamagnetic behavior as inferred from the vertical ridge near $B_c = 0$ mT that peaks around $B_u = 0$ mT. Although the peak coercivity range of our surface specimen is lower than that of the interior specimen, overall the domain structure of the specimen appears broadly similar. Therefore, domain state does not appear to account for the differences we find in paleointensity.

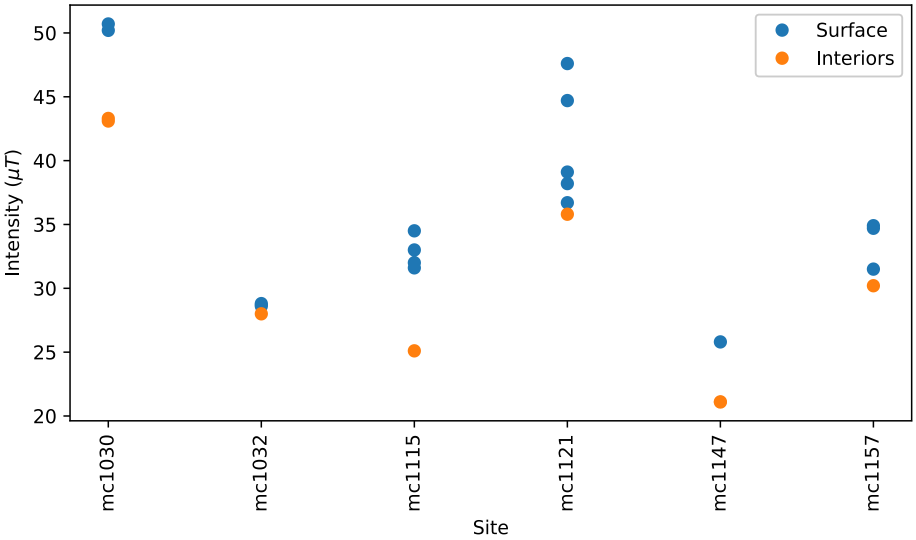

Figure 6. Paleointensity estimates from sites that pass CCRIT and include data from both the lava flow top (blue circles) and the lava flow interior (orange circles).

Table 4
Successful Paleodirection Results

Site	*k*	*N*	Dec (°)	Inc (°)	α_{95} (°)	VGP Lat (°)	VGP Lon (°)	Lat (°)	Lon (°)	Age (Ma)
Continued on next page mc1001	356	6	255.3	79.7	3.55	69.49	275.43	−77.85	166.64	1.18 ± 0.01
mc1002	290	6	334.4	−79.1	3.93	78.61	114.74	−77.85	166.69	0.33 ± 0.02
mc1008	361	8	39.4	−77.6	2.92	73.85	233.48	−77.80	166.83	0.65 ± 0.05
mc1009	192	8	253.8	−82.8	4.00	68.81	26.53	−77.55	166.20	0.07 ± 0.02
mc1010	217	7	335.9	−77.6	4.11	76.61	120.83	−77.57	166.23	
mc1011	452	8	325.2	−76.8	2.61	73.59	107.24	−77.57	166.23	
mc1014	450	8	0.5	−80.6	2.61	84.16	170.66	−77.46	169.23	
mc1015	949	9	172.2	84.6	1.67	87.61	26.42	−77.47	169.23	1.33 ± 0.02
mc1020	128	7	137.9	−79.3	5.34	59.24	317.40	−77.88	165.02	0.77 ± 0.032
mc1021	301	8	333.1	80.5	3.20	60.56	329.58	−78.21	166.49	
mc1029	106	6	25.2	−78.5	6.52	77.47	212.51	−78.31	164.80	0.18 ± 0.08
mc1030	140	8	242.5	68.8	4.69	56.23	242.70	−78.34	164.87	
mc1032	168	7	266.1	−75.3	4.66	59.48	49.92	−78.36	164.30	0.0078 ± 0.012
mc1033	381	8	9.6	−74.5	2.84	72.39	179.81	−78.38	164.34	
mc1034	393	7	281.6	−82.2	3.05	72.85	45.41	−78.39	164.27	0.3447 ± 0.0445
mc1035	316	8	301.6	−84.7	3.12	79.22	40.38	−78.39	164.23	0.12 ± 0.02
mc1036	171	7	348.7	−82.2	4.63	85.40	123.78	−78.39	164.27	0.12 ± 0.02
mc1037	316	8	215.6	81.6	3.12	80.27	242.85	−78.40	164.27	4.47 ± 0.04
mc1038	227	7	295.7	−77.9	4.02	69.23	71.27	−78.40	164.21	
mc1039	371	7	282.7	−87.3	3.14	78.34	11.16	−78.39	164.21	0.08 ± 0.01
mc1040	215	7	194.4	−83.0	4.12	64.85	352.17	−78.39	164.20	
mc1041	144	6	270.5	−78.3	5.59	64.85	48.78	−78.39	164.20	0.28 ± 0.02
mc1043	104	6	280.5	−85.1	6.57	76.31	28.83	−78.37	164.24	
mc1044	161	8	325.2	−74.1	4.37	68.86	112.55	−78.36	164.26	
mc1048	229	6	75.8	−54.9	4.43	37.46	247.79	−78.24	163.36	
mc1100	163	6	12.6	−74.3	5.26	71.94	182.97	−78.30	162.90	0.86 ± 0.23
mc1101	863	6	35.8	−79.1	2.28	76.69	228.48	−78.31	162.93	1.07 ± 0.01
mc1103	220	7	136.7	71.2	4.07	63.25	104.41	−78.24	163.36	1.42 ± 0.03
mc1104	236	6	69.0	−75.5	4.37	64.56	256.04	−78.24	163.40	0.29 ± 0.02
mc1106	434	6	18.4	−76.3	3.22	74.72	194.98	−78.21	163.31	13.42 ± 0.18
mc1107	783	6	95.5	−84.5	2.40	73.27	302.68	−78.20	163.35	2.57 ± 0.38
mc1109	661	6	172.6	76.0	2.61	74.98	150.65	−78.28	163.54	1.26 ± 0.04
mc1110	245	6	253.4	80.0	4.28	70.49	270.66	−78.24	163.44	7.94 ± 0.24
mc1111	1193	7	47.9	−67.8	1.75	57.63	224.04	−78.22	162.79	1.99 ± 0.04
mc1112	159	6	232.9	74.4	5.31	66.17	237.62	−78.24	163.44	7.63 ± 0.32
mc1113	130	7	257.0	77.6	5.30	66.13	266.80	−78.23	162.74	6.73 ± 0.17
mc1115	222	6	74.9	67.5	4.50	46.10	45.51	−78.24	162.96	2.46 ± 0.31
mc1116	157	6	275.6	−80.7	5.36	69.44	44.86	−78.22	162.74	1.14 ± 0.11
mc1117	1152	6	169.0	68.9	1.97	63.85	147.72	−78.24	162.97	2.28 ± 0.24
mc1118	108	7	58.6	−52.2	5.82	38.27	229.23	−78.24	163.14	0.31 ± 0.04
mc1119	966	6	126.3	48.4	2.16	35.80	102.92	−78.24	162.96	1.08 ± 0.22

Table 4
Continued

Site	k	N	Dec (°)	Inc (°)	α_{95} (°)	VGP Lat (°)	VGP Lon (°)	Lat (°)	Lon (°)	Age (Ma)
mc1120	624	9	72.4	−70.5	2.06	56.59	252.58	−78.24	163.09	1.76 ± 0.05
mc1121	641	10	117.8	79.1	1.91	71.47	68.16	−78.24	162.95	2.51 ± 0.06
mc1123	296	8	75.8	−82.5	3.22	73.59	282.42	−78.25	163.73	1.93 ± 0.05
mc1124	385	6	15.2	−72.7	3.42	69.26	186.58	−78.19	163.57	12.61 ± 0.11
mc1125	153	7	342.6	−63.7	4.89	56.39	141.47	−78.25	163.73	4.26 ± 0.18
mc1126	305	7	12.7	−77.9	3.46	77.99	188.33	−78.25	163.74	
mc1127	689	8	325.3	−66.9	2.11	58.62	118.62	−78.25	163.73	1.94 ± 0.07
mc1128	370	8	33.4	−80.8	2.88	79.67	237.79	−78.21	166.57	8.75 ± 0.03
mc1130	257	6	150.1	46.3	4.18	37.66	132.63	−78.21	166.58	7.25 ± 0.07
mc1131	398	8	20.8	−58.6	2.78	50.15	192.03	−78.21	166.57	9.66 ± 0.18
mc1133	305	6	38.8	−85.6	3.84	82.63	298.22	−78.20	166.58	
mc1134	1049	6	11.8	−84.2	2.07	87.60	267.63	−78.22	166.61	9.02 ± 0.05
mc1135	209	8	266.3	−77.6	3.83	62.95	48.78	−78.23	166.56	3.6 ± 0.01
mc1139	892	6	169.8	79.0	2.24	80.05	141.19	−78.26	163.08	0.88 ± 0.08
mc1140	553	6	343.7	−78.7	2.85	79.03	129.91	−78.28	163.00	2.03 ± 0.09
mc1141	100	6	91.4	83.4	6.71	72.36	150.00	−77.58	−77.58	1.31 ± 0.02
mc1142	355	9	318.5	85.3	2.73	69.82	328.38	−77.85	166.68	1.23 ± 0.02
mc1143	188	6	29.8	−52.1	4.90	42.70	197.51	−78.24	162.88	2.08 ± 0.65
mc1144	108	7	198.4	79.6	5.83	80.63	208.42	−77.85	166.69	
mc1145	773	6	27.6	2.6	2.41	9.12	190.86	−78.24	162.89	1.9 ± 0.12
mc1146	122	7	236.1	63.2	5.48	50.34	230.48	−78.22	162.96	1.37 ± 0.42
mc1147	361	6	220.3	64.3	3.53	54.44	213.47	−78.20	162.96	1.63 ± 0.34
mc1148	104	6	283.6	−79.6	6.58	69.09	56.82	−77.49	167.25	0.72 ± 0.66
mc1152	887	6	333.2	−85.6	2.25	84.02	23.24	−77.72	162.65	3.87 ± 0.15
mc1153	161	6	311.2	57.9	5.29	29.98	299.36	−77.76	162.14	2.53 ± 0.13
mc1154	514	6	283.1	87.7	2.96	75.98	324.02	−77.72	162.63	2.19 ± 0.08
mc1155	212	8	230.1	78.1	3.81	72.47	243.37	−77.70	162.25	1.5 ± 0.05
mc1156	381	6	162.7	72.7	3.43	69.56	135.88	−77.70	162.59	1.89 ± 0.13
mc1158	971	6	48.6	43.7	2.15	17.07	27.60	−77.69	162.46	3.74 ± 0.25
mc1160	214	8	233.5	77.8	3.79	71.23	245.95	−77.69	162.35	3.47 ± 0.05
mc1164	1255	7	201.6	85.6	1.70	84.59	312.77	−77.51	169.33	1.36 ± 0.01
mc1165	151	6	159.2	79.6	5.45	80.45	121.68	−77.51	169.33	1.45 ± 0.06
mc1167	6080	8	186.2	72.5	0.71	70.11	179.11	−77.49	169.29	
mc1168	197	7	183.7	67.7	4.30	63.16	174.45	−77.49	169.29	1.38 ± 0.05
mc1170	1621	6	2.2	−87.5	1.66	82.76	345.19	−77.85	166.71	1.03 ± 0.1
mc1200	342	6	301.9	−84.8	3.62	78.81	38.42	−77.55	166.16	0.07 ± 0.01
mc1201	347	6	257.4	−79.7	3.60	64.35	36.72	−77.56	166.22	0.09 ± 0.01
mc1202	3487	6	341.2	−46.6	1.13	39.48	144.75	−77.66	166.36	0.54 ± 0.01
mc1205	579	9	283.4	−34.2	2.14	21.20	85.69	−77.66	166.73	0.37 ± 0.02
mc1206	147	9	326.2	−32.6	4.26	27.79	129.99	−77.67	166.78	
mc1207	334	6	46.0	−71.2	3.67	62.99	229.63	−77.68	166.52	0.5187 ± 0.0043

Table 4
Continued

Site	k	N	Dec (°)	Inc (°)	α_{95} (°)	VGP Lat (°)	VGP Lon (°)	Lat (°)	Lon (°)	Age (Ma)
mc1208	256	6	38.3	−66.2	4.19	57.45	216.21	−77.67	166.53	
mc1209	473	6	59.2	−62.7	3.08	49.29	237.50	−77.69	166.37	0.7828 ± 0.0667
mc1210	1141	6	51.6	−69.4	1.98	59.36	233.89	−77.69	166.37	
mc1211	617	8	4.8	−55.5	2.23	48.36	172.17	−77.66	166.34	
mc1214	1575	10	176.2	77.8	1.22	79.35	158.17	−77.22	166.43	3.88 ± 0.04
mc1215	268	8	347.8	−82.4	3.38	86.26	110.24	−77.48	166.89	0.34 ± 0.02
mc1217	114	10	287.0	−71.9	4.54	58.43	74.76	−77.51	167.44	0.16 ± 0.01
mc1218	132	6	343.4	−81.5	5.84	84.10	114.26	−77.56	166.98	0.03 ± 0.01
mc1220	391	10	36.8	−82.4	2.44	81.15	260.37	−77.46	166.91	0.53 ± 0.04
mc1221	454	6	274.1	−82.9	3.15	72.06	37.94	−77.52	166.80	0.12 ± 0.01
mc1222	307	6	190.4	−52.1	3.83	20.45	356.14	−77.54	166.85	0.11 ± 0.01
mc1223	161	9	59.8	−82.6	4.06	76.53	277.72	−77.66	166.79	0.38 ± 0.03
mc1224	568	6	192.0	−61.0	2.81	29.86	357.10	−77.53	166.88	0.03 ± 0.01
mc1225	1052	6	113.8	−74.6	2.07	54.46	297.40	−77.58	166.80	0.06 ± 0.01
mc1226	1468	6	19.3	−50.6	1.75	42.93	189.46	−77.61	166.77	0.24 ± 0.02
mc1227	2347	6	221.2	61.8	1.38	51.92	218.00	−77.27	166.73	2.32 ± 0.02
mc1228	161	10	212.2	67.7	3.81	60.68	210.15	−77.27	166.38	
mc1229	339	8	99.5	73.1	3.01	58.57	65.93	−77.48	167.15	1.07 ± 0.18
mc1301	707	6	134.2	77.4	2.52	72.13	209.25	−78.22	−78.22	
mc1302	368	11	102.5	−73.9	2.38	55.68	41.92	−78.19	−78.19	0.04 ± 0.01
mc1303	263	17	17.8	−55.1	2.20	47.33	303.94	−77.58	−77.58	1.31 ± 0.02
mc1304	198	13	156.5	75.6	2.95	73.03	243.19	−78.24	−78.24	0.29 ± 0.02
mc1305	482	16	191.3	71.1	1.68	67.07	298.26	−78.24	−78.24	0.9 ± 0.1
mc1306	175	12	171.4	57.1	3.28	49.81	271.69	−77.70	−77.70	2.56 ± 0.13
mc1307	367	18	226.1	75.5	1.81	69.34	351.67	−77.85	−77.85	1.33 ± 0.12

Note. κ, precision parameter; N, successful cores per site; Dec, declination (°); Inc, inclination (°); α_{95}, circle of 95% confidence; VGP Lat, virtual geomagnetic pole latitude (°); VGP Lon, virtual geomagnetic pole longitude (°); Lat, site latitude; Lon, site longitude; Age, Age (Ma). Site names were modified for this study. Sites from Mankinen and Cox (1988) (mc1-50) are renamed mc1001-mc1050 while those from Lawrence et al. (2009) (mc100-mc229) are renamed mc1100-mc1229. Sites that were recombined for this study are labeled mc1301-mc1307.We have included the results from an additional 30 sites that passed our directional criteria yet exceeded our 5 million years age cut-off.

3.4. ^{40}Ar/^{39}Ar Geochronology

Several sites were formerly radiometrically dated (Esser et al., 2004; Lawrence et al., 2009; Tauxe et al., 2004; Wilch et al., 1993). We selected an additional 13 sites for ^{40}Ar/^{39}Ar age analysis (see Table S2) based on the promising sites from our preliminary study. Site ages were determined by their plateau age. Each plateau age estimate includes over 60% of the $^{39}Ar_k$ released, excluding sites mc1034, mc1131, and mc1157 which only include 52%, 50%, and 44% of the $^{39}Ar_k$ released, respectively (Figure 8). Samples give plateau ages that are concordant with their inverse isochron ages. Two samples from site mc1033 yield significantly different age estimates, so we exclude both ages.

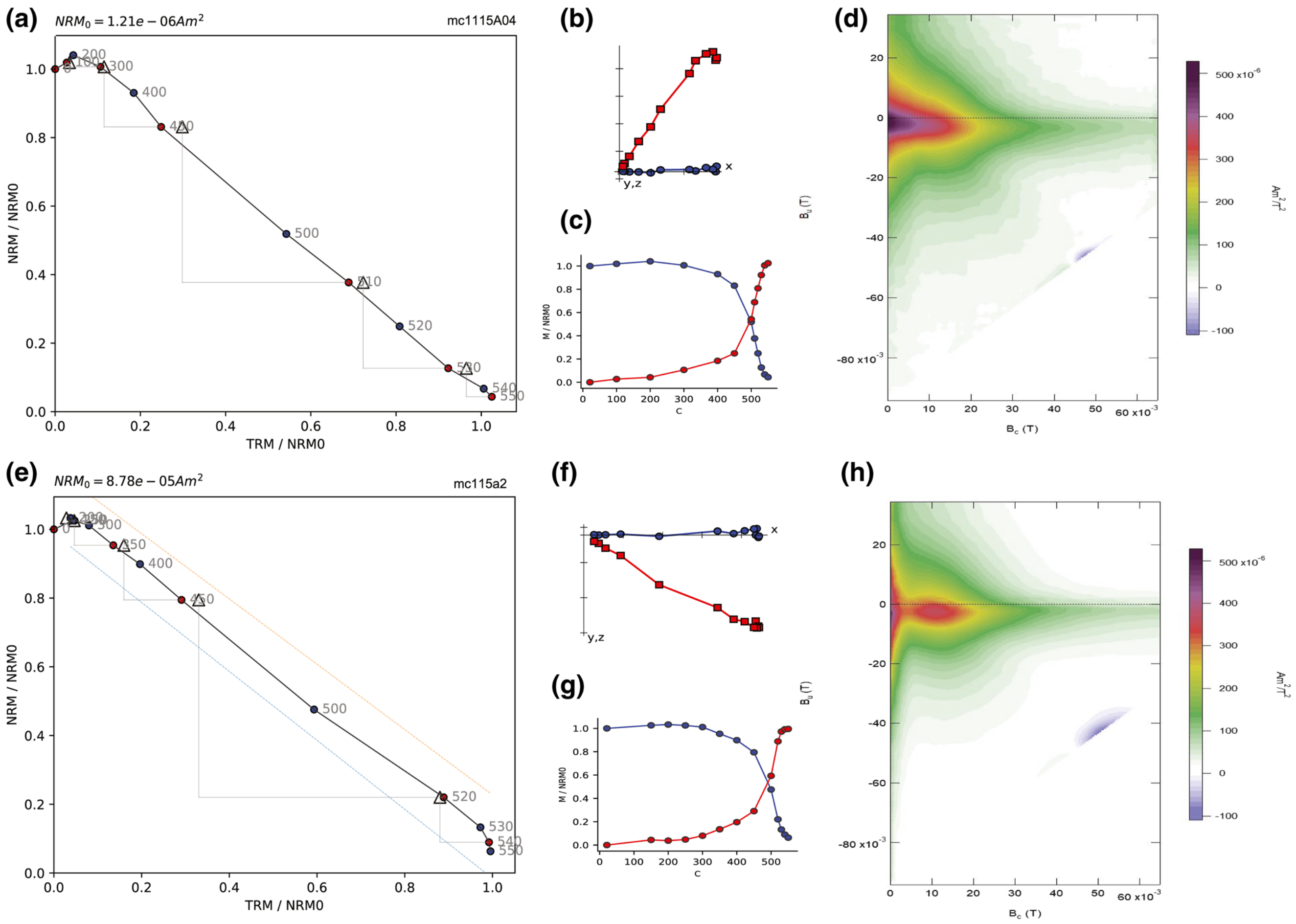

Figure 7. Arai diagram (a, e), Zijderveld diagram (b, f), MT (magnetization-temperature) curve (c, g), and FORC diagrams (d, h) for samples from site mc1115 that passed CCRIT. Specimen mc115A04 (a–d) was sampled from the lava flow top and yielded a 31.55 μT paleointensity while mc115a2 (e–h) was collected from the lava flow interior and estimated a 25.15 μT paleointensity.

4. Discussion

4.1. Examining the GAD Structure of the Ancient Magnetic Field

4.1.1. Paleointensities

Our new paleointensity data set consists of 26 sites from the Plio-Pleistocene that pass CCRIT (Table 3). We converted the paleointensities to their corresponding virtual axial dipole moments (VADMs) to compare intensity estimates across latitudes (Figure 9c). VADM is the strength of the axial dipole moment that would generate the intensity observed at a given latitude. Our 26 sites yield an average intensity of 33.57 ± 2.71 μT or equivalently an average PADM of 44.18 ± 3.57 ZAm^2. We find similar PADMs for the Brunhes chron (44.94 ± 4.18 ZAm^2) and the Matuyama chron (41.54 ± 5.52 ZAm^2). Our average intensity estimate is slightly higher than that of Lawrence et al. (2009) and about half of the modern intensity measured in the Erebus Volcanic Province (~62 μT). This is consistent with predictions of an average dipole moment of ~42–50 Am^2 (e.g., Juarez et al., 1998; Selkin & Tauxe, 2000; Tauxe et al., 2013; Wang et al., 2015) over the long term. However, there remains the problem that the data from the last few million years from the global data set show no dependence of field strength on latitude (Figure 2) which, if true, belies the existence of a single GAD moment sampled by all the studies.

To assess the structure of the paleomagnetic field over the Plio-Pleistocene, we compare our results to globally distributed paleointensity data stored in the PINT database (Biggin et al., 2009). While our estimated

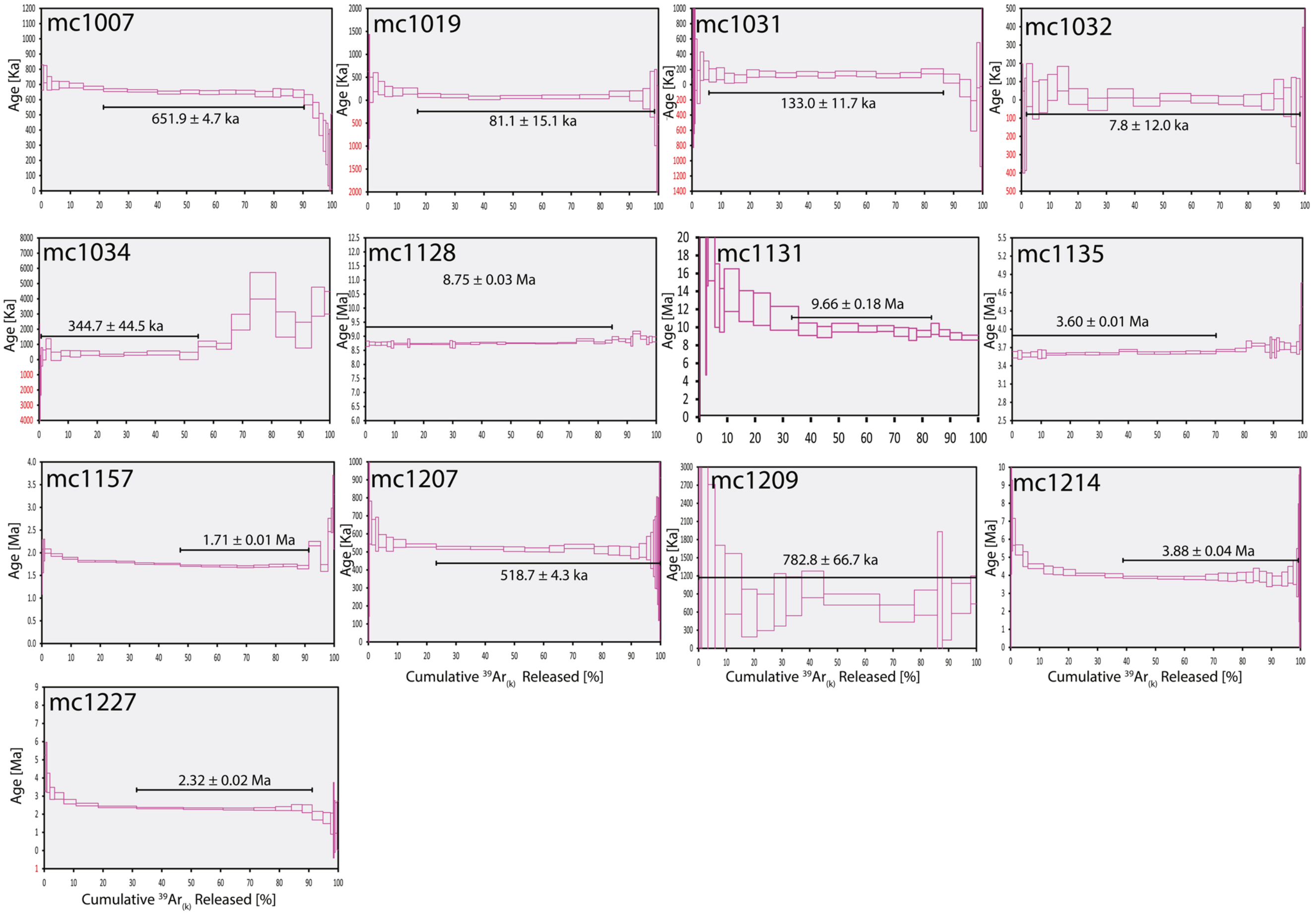

Figure 8. Results from the ^{40}Ar/^{39}Ar incremental heating method used to date 13 sites. Black bars mark the bounds of the age spectra plateau that were used to estimate the site age.

PADM of 44.13 ± 3.57 ZAm^2 is consistent with many recent estimates for the long term average (e.g., Juarez et al., 1998; Selkin & Tauxe, 2000; Tauxe et al., 2013; Wang et al., 2015; Ziegler et al., 2011), our intensity estimate at the high southerly latitudes, when compared to the global data set, does not display the latitudinal dependence of intensity expected of a GAD generated field (Figure 2) and appears depressed when compared to the global paleointensity data set over the Plio-Pleistocene.

Our results yield a PADM of ~44 ZAm^2, which is substantially weaker than the modern dipole moment of ~77 ZAm^2. Given this weaker dipole, we would expect to recover even lower intensities at lower latitude sites (~15 μT at the equator) but this is not the case in the global Plio-Pleistocene dataset. Although a few recent studies (Wang et al., 2015) have published results in agreement with this prediction, many older studies from mid and low latitudes have much higher values (Figure 2) than predicted by a PADM of ~40–50 ZAm^2.

As discussed by Lawrence et al. (2009), the reasons for the lack of a dipole signal in the global data set are not clear. The results from some experimental protocols may be biased (e.g., Cai et al., 2017; Cromwell et al., 2018). A bias in temporal sampling toward the present could also cause a high bias in the median intensity because more recent data appear to have higher intensities (Constable et al., 2016; Selkin & Tauxe, 2000; Ziegler et al., 2011). Sampling material may also affect paleointensity estimates. Selkin and Tauxe (2000) recovered the expected latitudinal dependence of paleointensity, with a PADM of ~44 ZAm^2, by examining paleointensities solely from submarine basalt glass. Submarine basalt glass forms by rapid cooling and therefore it may be more likely to contain SD particles. In the following section we explore the effect of sampling material on the resulting paleointensity estimate.

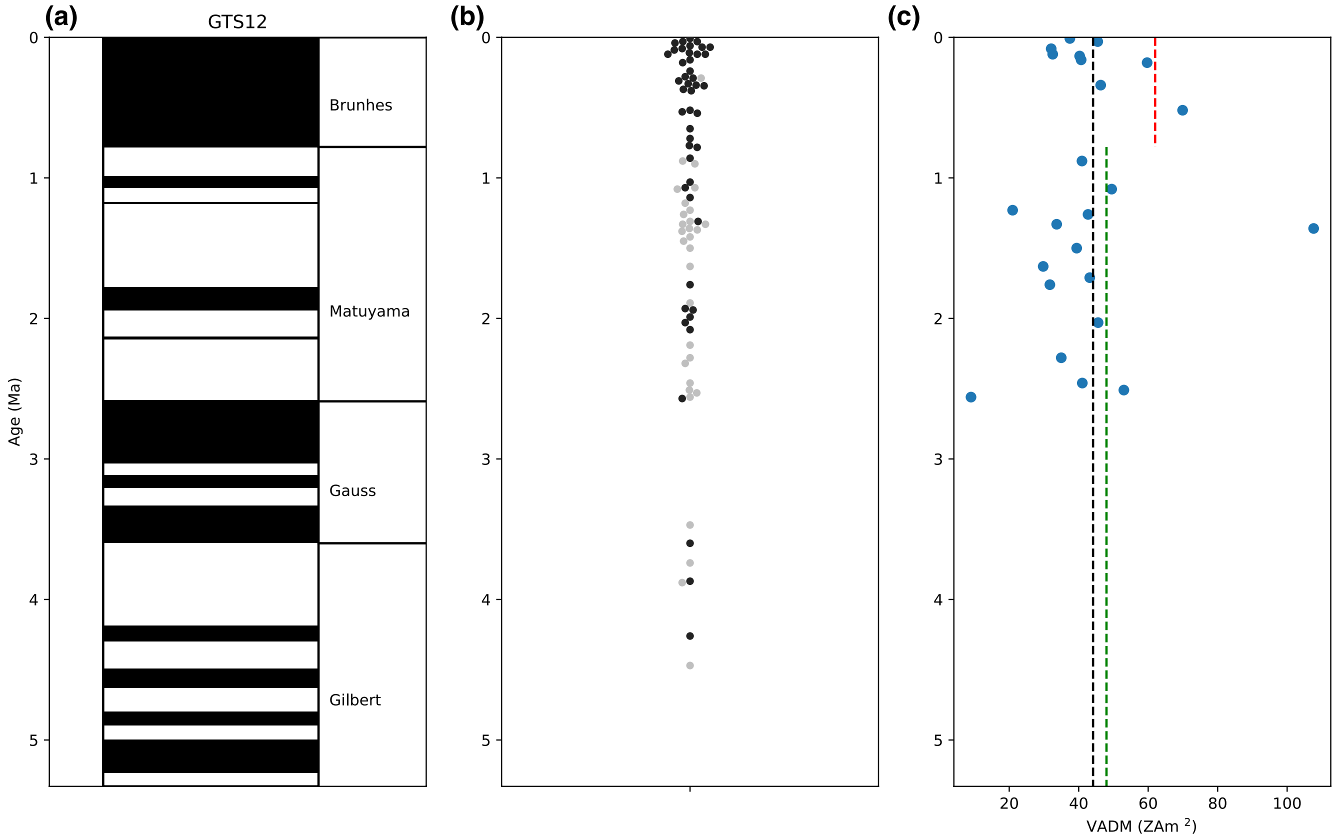

Figure 9. (a) The 2012 Geomagnetic Polarity Timescale for the Plio-Pleistocene (Gradstein et al., 2012). (b) The distribution of ages for our sites, colored by normal (black) and reverse (gray) polarity. (c) The distribution of VADM computed in this study. The red (green) dashed line is the PADM from Zeigler et al. (2011) for the Brunhes (Matuyama). The black dashed line is the average PADM for this study. PADM, paleomagnetic axial dipole moment; VADM, virtual axial dipole moment.

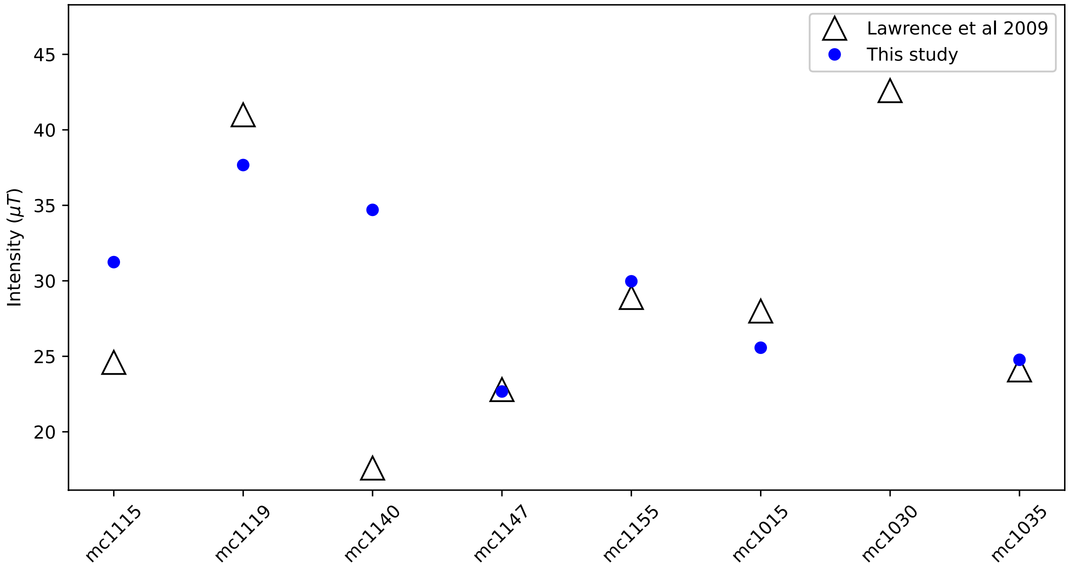

Figure 10. Average intensity estimates for the sites in this study that passed CCRIT (blue circles) and the sites from Lawrence et al. (2009) (white triangles) that passed their set of selection criteria.

Table 5
Paleodirectional Results From This Study

Polarity	*N*	Dec (°)	Inc (°)	VGP Lon (°)	VGP Lat (°)	α_{95} (°)
Normal polarity intervals	62	2.5	−81.6	159.2	88.4	7.1
Reverse polarity intervals	36	1.5	−81.1	225.0	85.3	9.0
Combined	98	2.1	−81.4	201.9	87.7	5.5

Note. *N*, number of sites; Dec, declination; Inc, inclination; VGP Lon, VGP longitude; VGP Lat, VGP latitude; α_{95}: 95% confidence bounds.

4.2. Examining the Role of Sampling Material

In Figure 10, we compare results from our sites that passed CCRIT with the original interpretations of Lawrence et al. (2009). A few sites (mc1147, mc1155, mc1015, and mc1035) yield intensity estimates within a few μT of each other, while others (mc1115, mc1119, and mc1140) vary by up to ±15 μT. Six of the original sites have specimens that passed CCRIT and include specimens from both the interior and the surface of the same lava flow. We assume that a single lava flow cooled quasi-instantaneously, so the surface and interior of the flow should preserve identical intensities. However, as shown in Figure 6, specimens from the interior yield systematically lower paleointensities than those from the flow top by 2–8 μT.

Figure 6 suggests that specimens from lava interiors, when subjected to the same selection criteria, yield lower paleointensity estimates than those collected from the lava flow surfaces. Assuming that the interiors cooled more slowly, we considered the possibility that a difference in cooling rate effected the original magnetization (Dodson & McClelland-Brown, 1980; Santos & Tauxe, 2019) causing the difference in intensity estimates. For SD grains, we would expect that a slower cooling rate may result in a higher intensity of magnetization (Dodson & McClelland-Brown, 1980; Santos & Tauxe, 2019). We tested the effect of cooling rate on the TRM of the specimens by conducting a cooling rate experiment. Each specimen preserved a higher remanence following slow cooling than fast cooling as expected from SD theory (see Figure S5). Therefore, differences in the cooling history between the two sampling regions (i.e., that the flow tops cooled more quickly than the flow interiors) does not explain the lower paleointensities we measure in the interior.

Next, we tested whether differences in domain state or magnetic interaction could explain the behavior by measuring hysteresis loops and FORC diagrams (Pike et al., 1999). The magnetic moments in specimens from mc1115 (Figure 7) and mc1147 (see Figure S6) include a superparamagnetic component, a SD component and some degree of interaction (Roberts & Verosub, 2000). The specimen from the surface appears to have a greater contribution from lower coercivity grains than their counterparts from the interior. But overall, the domain structure of specimens from the interiors appears broadly similar to those from the flow tops at the same site for the specimens that passed CCRIT. Therefore, differences in domain states do not account for the higher paleointensities measured in the samples collected from the surface.

In addition to cooling rate and domain state, we investigated whether nonlinear TRM acquisition could explain the bias in the intensity estimates from the interior. Our samples, collected from the surface during the 2016/2017 field season, were treated in a 30 μT field during the in-field steps of the IZZI experiment. Lawrence et al. (2009) cooled some specimens from the interior in a 25 μT field and other specimens in a 30 μT field. We investigate whether the lower intensities measured in the interiors resulted from the lower intensities applied during the IZZI experiment by testing for nonlinearity. We performed TRM acquisition tests in fields ranging from 0 to 60 μT (Figure S7). All specimens showed linear behavior with applied field. Thus, neither cooling rate, domain state, nor nonlinear TRM acquisition accounts for the lower intensities recorded by the specimens sampled from the interior of the lava flows. Only 6 of our 26 successful sites include paleointensity estimates from both the surface and the interior of the lava flow. We believe the intensity estimates that pass CCRIT from both contexts preserve reliable intensity estimates. A full investigation on the role of sampling material on paleointensity estimates would require a larger sample size.

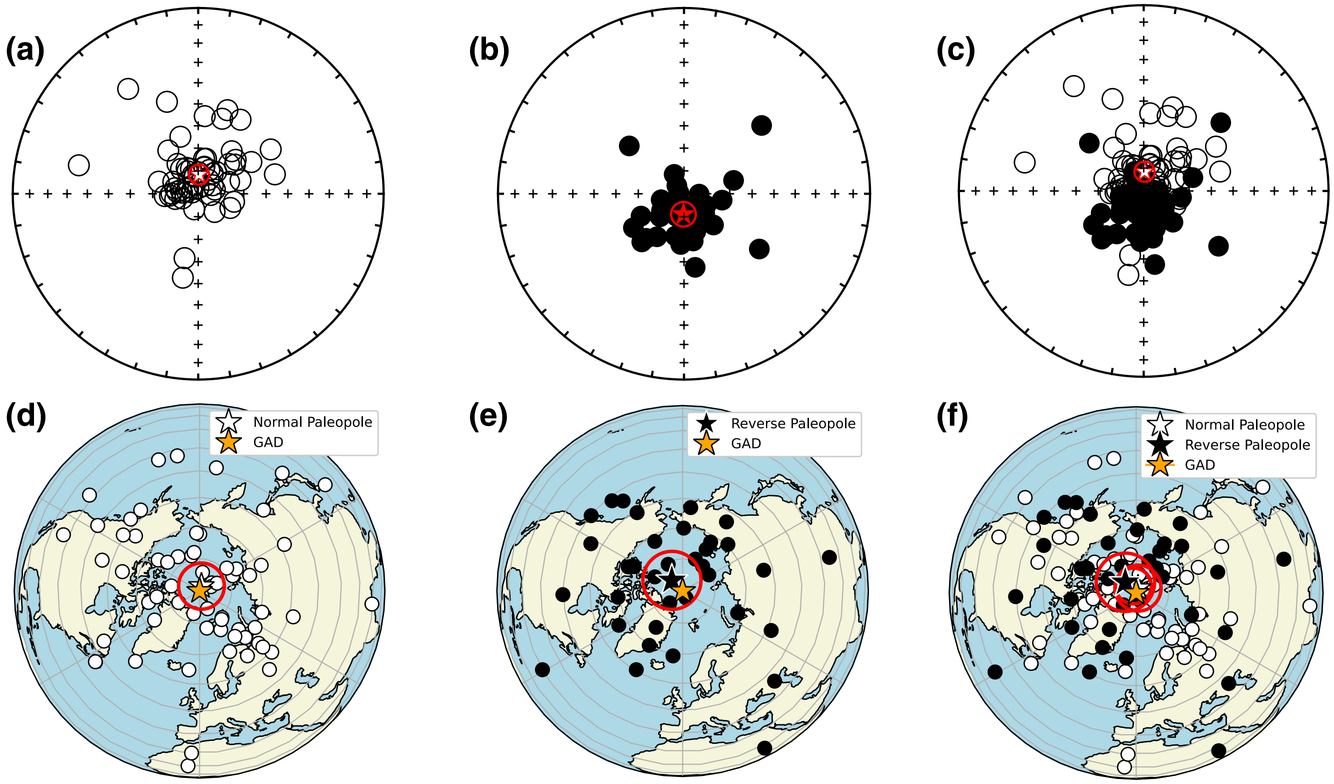

Figure 11. (a–c) Equal area projections of the site mean directions that passed our selection criteria along with their corresponding α_{95} (red circles). Upward (lower) hemisphere projections are open (closed) circles. (a) Normal polarity directions, (b) reverse polarity directions, and (c) all directions. (d–e) Maps of the VGPs (circles). The paleopole for the normal (reverse) polarity interval is marked with a white (black) star. The GAD is marked as an orange star. Red circles around the paleopole mark α_{95}s. (d) The normal polarity interval (directions in a and e) the reverse polarity interval (directions in b), and (f) the entire data set (directions in c); the reverse polarity data (black circles) are flipped to the antipode. GAD, geocentric axial dipole; VGP, virtual geomagnetic pole.

4.2.1. Paleodirections

4.2.1.1. Paleopole. We have combined our new directional data measured for this study with the data of Lawrence et al. (2009) (see Table S1 for combined sites) and (re)analyzed all of the directional data. Our new data set consists of 98 site-mean directions that pass our selection criteria (Table 4). It includes 62 normal polarity (Figure 11a) and 36 reverse polarity (Figure 11b) site-mean directions (Table 5). We applied a bootstrap reversal test (Tauxe et al., 1991) on the reverse and normal polarity directions. The directions pass the reversal test, so the two sets are indistinguishable (see Figure S2) and we can combine the antipodes of the reverse polarity directions with the normal polarity directions and analyze the combined data set.

A virtual geomagnetic pole (VGP) is the coordinates of the geocentric magnetic dipole that would generate the direction measured at a particular location. The paleomagnetic site-mean directions were transformed to their corresponding VGPs (Figure 11d–11f). We calculated the paleomagnetic pole and α_{95} (Fisher, 1953) by taking the average of the VGPs for the normal polarity sites in Figure 11d (159.2°, 88.4°, and α_{95} 7.08°), the antipode of the reverse polarity sites in Figure 11e, (225.0°, 85.3°, and α_{95} 9.02°) and for the combined data set in Figure 11f (201.9°, 87.7°, and α_{95} 5.5°), see Table 5. The 95% confidence bounds of each paleopole includes the spin axis, so the paleodirections from our study are consistent with a GAD field.

Table 6
S: VGP Dispersion, S_{45}: VGP Dispersion for the Data Filtered by a 45° VGP Cut-Off, and S_{vand}: VGP Dispersion for the Data Filtered by the Vandamme Cut-Off

	S	N_S	S_{45}	N_{S45}	S_{vand}	N_{Svand}
Normal	$30.56^{33.54}_{26.98}$	62	$22.98^{25.28}_{20.40}$	53	$26.46^{30.03}_{20.86}$	58
Reverse	$29.82^{35.01}_{24.67}$	36	$24.55^{26.67}_{20.68}$	33	$24.55^{31.57}_{20.55}$	33
Combined	$30.14^{33.61}_{26.78}$	98	$23.45^{24.91}_{21.51}$	86	$24.26^{28.35}_{21.55}$	88
Brunhes	$32.50^{38.79}_{25.20}$	31	$21.44^{24.25}_{18.36}$	25	$26.16^{37.71}_{19.08}$	28
Matuyama	$29.32^{32.65}_{25.21}$	38	$26.03^{28.59}_{23.01}$	35	$27.99^{32.90}_{22.66}$	37
Gilbert	$35.98^{53.51}_{14.69}$	7	$22.15^{28.10}_{11.85}$	6	$22.15^{48.85}_{15.72}$	6
TK03	$23.49^{28.49}_{19.72}$	98[a]	$19.66^{21.61}_{17.59}$	98[a]	$18.77^{21.49}_{15.97}$	98[a]

Note. Beside the VGP dispersion is the bootstrap upper (top) and lower (bottom) 95% confidence bounds for each set of VGPs.

[a] Bootstrapped 1,000 times.

4.2.1.2. VGP dispersion. In addition to testing the GAD hypothesis by comparing the paleopole from this study with the coordinates of the spin axis, we can test the variability of the geomagnetic field, PSV, over the Plio-Pleistocene by calculating the dispersion of the VGPs about the geographic pole (McElhinny, 1973). VGP dispersion quantifies the scatter in the site-level VGP estimates. The scatter within each site will vary based on the directions selected to calculate the VGP. At the site-level, we set the number of cores per site (N) to ≥6 and the precision parameter (k) to ≥100 as our criteria to minimize VGP dispersion without discarding too many sites, N, that fail to meet these criteria (Table 4). Although the within-site scatter differs between sites, we assume that the N and k cut-offs account for this variability, and so we quantify VGP dispersion using S (Cox, 1970):

$$S^2 = (N-1)^{-1}\sum_{i=1}^{N}(\Delta_i)^2 \tag{5}$$

where N is the number of sites and Δ_i is the angular deviation between the ith VGP and the spin axis. We calculate S for the normal polarity poles, the reverse polarity poles, and the combined data set which includes the antipodes of the reverse polarity poles and the normal polarity poles that passed our set of selection criteria (Table 6). We also calculate the 95% bootstrap upper and lower confidence bounds for the VGP dispersion of each data set. The VGP dispersion is higher for the normal polarity poles than the reverse polarity poles but both results fall within the overlapping 95% bootstrap confidence bounds of the two data sets so the difference in VGP dispersion is insignificant.

VGP cut-offs were introduced to exclude VGPs with low latitudes from the calculation of dispersion (Watkins, 1973). Low-latitude VGPs may reflect directions acquired during unstable transitional or excursional field states. S_{45} filters the VGPs that passed our selection criteria with a strict 45° VGP cut-off. Applying this 45° VGP cut-off, reduces dispersion by 5°–8°. The VGP dispersion is higher in the reverse polarity poles than the normal polarity poles, but once again the poles fall within their overlapping 95% bootstrap confidence bounds so the difference is not significant. We also filter the original VGP data set with the Vandamme cut-off (Vandamme, 1994), S_{vand}, which applies an iterative VGP cut-off. Applying this VGP filter also reduces the VGP dispersion. Both cut-offs result in comparable estimates for dispersion, although S_{vand} filters slightly fewer sites. Although a VGP cut-off may remove transitional/excursional field directions, it may also underestimate dispersion by excluding "normal" secular variation, particularly at high latitudes where the scatter is high. For example, a strict 45° VGP cut-off would bias against paleodirections recovered from high latitudes because there is a latitudinal dependence of dispersion-higher latitudes record higher dispersion (McFadden et al., 1988).

Our results include paleodirections from the Plio-Pleistocene, including many from the Brunhes, Matuyama, and Gilbert Chrons (see Figures 9a and 9b). We test whether dispersion varies between chrons by filtering our data set by age and calculating the dispersion and 95% bootstrap confidence bounds of each chron separately. Our data set includes a single VGP from the Gauss chron so we exclude this chron from our calculation. For both filtered and unfiltered VGPs, the dispersion falls within the overlapping 95% bootstrap confidence interval (see Figure S4), so our data set suggests there is no distinction in VGP dispersion between chrons.

We compare our dispersion data to two PSV models: Model G (McFadden et al., 1988) and TK03 (Tauxe & Kent, 2004). Model G predicts VGP scatter according to:

$$S = \sqrt{A^2\lambda^2 + B^2} \tag{6}$$

where $A = 0.21$ and $B = 13.6$ for the last 5 Ma from (McFadden et al., 1988). Model G therefore predicts the dispersion at −78° as 21.3° which fits our 45° or Vandamme cut-off estimates of dispersion fairly well. However, Model G underestimates the unfiltered dispersion data at our high southern latitude study. We also compare the results from our data set to estimates of dispersion from a set of directions drawn from the statistical PSV model, TK03. We drew a set of directions from the centroid position of our sites (78.22°S, 164.34°E), transformed the directions to their corresponding VGPs, and then calculated dispersion for the synthetic data set. We repeated these steps 1,000 times for an S of $23.49^{28.49}_{19.72}$. The dispersion of our S_{45} and S_{vand} filtered VGPs is consistent with our unfiltered estimate of dispersion from the statistical PSV model

TK03. The bounds on the unfiltered VGPs overlap with the bootstrapped 95% confidence interval of our TK03-derived dispersion. Based on our results, dispersion appears consistent between normal and reverse polarities, consistent between the Brunhes and Matuyama chron, and higher than, but within error of the VGP dispersion predicted by TK03 (Tauxe & Kent, 2004). We note that other Giant Gaussian Process models (i.e., Bono et al., 2020, BB18-family) could provide a better fit by estimating higher dispersion at high latitudes.

5. Conclusions

We present an extensive study of the paleomagnetic field over the Plio-Pleistocene in the Erebus Volcanic Province, Antarctica (−77.84°, 166.69°) and 13 new ^{40}Ar/^{39}Ar results. We recovered a paleopole at 201.9°, 87.7° from 98 independent sites that were subjected to either thermal or AF demagnetization and then filtered using a set of strict selection criteria. The α_{95} of the paleopole is 5.5° and encompasses the spin axis so the paleodirections measured from the EVP during the Plio-Pleistocene are consistent with a GAD field. In addition, we conducted an IZZI-modified Thellier-Thellier experiment and applied the CCRIT set of selection criteria to estimate paleointensity. Twenty-six sites passed our criteria and recorded a $33.57 \pm 2.71\ \mu$T average intensity and a 44.13 ± 3.57 ZAm^2 average VADM. Compared to global paleointensity estimates stored in the PINT database, our results from Antarctica are lower than expected for a purely GAD field generated by a dipole with the present data value. We conclude that this lower intensity near the pole reflects weaker PDM. However, the possibility remains that there was a strongly non-GAD structure of the paleomagnetic field over the Plio-Pleistocene. To test this further, we must repeat this same study of Plio-Pleistocene paleomagnetic field at several latitudes (Dossing et al., 2016; Wang et al., 2015) to ensure adequate temporal overlap and high-quality paleointensity results.

Data Availability Statement

The data are available here https://earthref.org/MagIC/17076 and will be made public at: https://earthref.org/MagIC/17076 upon acceptance of this manuscript.

Acknowledgments
This work was funded by the National Science Foundation Grants OPP1541285 and EAR1827263. The first author gratefully acknowledges support by the National Science Foundation Graduate Research Fellowship under Grant no. DGE-1650112. The authors thank the United States Antarctic Program for their ground support in Antarctica. They also thank Christeanne Santos for her assistance with data collection and Cathy Constable, Jeff Gee, Shuhui Cai, and Nicole Behar for their helpful discussions. They are also grateful to their anonymous reviewers.

References

Aitken, M. J., Allsop, A. L., Bussell, G. D., & Winter, M. B. (1988). Determination of the intensity of the Earth's magnetic field during archeological times: Reliability of the Thellier technique. *Reviews of Geophysics*, *26*, 3–12.

Behar, N., Shaar, R., Tauxe, L., Asefaw, H., Ebert, Y., Heimann, A., & Hagai, R. (2019). Paleomagnetism and paleosecular variations from the plio-pleistocene Golan Heights volcanic plateau, Israel. *Geochemistry, Geophysics, Geosystems*, *20*, 4319–4334.

Ben-Yosef, E., Tauxe, L., Levy, T., Shaar, R., Ron, H., & Najjar, M. (2009). Geomagnetic intensity spike recorded in high resolution slag deposit in southern Jordan. *Earth and Planetary Science Letters*, *287*, 529–539.

Biggin, A. (2010). Paleointensity database updated and upgraded. *EOS*, *91*, 15.

Biggin, A., Strik, G., & Langereis, C. (2009). The intensity of the geomagnetic field in the late-Archean: New measurements and analysis of the updated IAGA palaeointensity database. *Earth Planets and Space*, *61*, 9–22.

Bono, R., Biggin, A., Holme, R., Davies, C., Meduri, D., & Bestard, J. (2020). Covariant giant Gaussian process models with improved reproduction of paleosecular variation. *Geochemistry, Geophysics, Geosystems*, *21*, e2020GC008960. https://doi.org/10.1029/2020GC008960

Cai, S., Tauxe, L., & Cromwell, G. (2017). Paleointensity from subaerial basaltic glasses from the second Hawaii Scientific Drilling Project (HSDP2) core and implications for possible bias in data from lava flow interiors. *Journal of Geophysical Research*, *122*, 8664–8674. https://doi.org/10.1002/2017JB014683

Coe, R. (1967). Paleo-intensities of the Earth's magnetic field determined from tertiary and quaternary rocks. *Journal of Geophysical Research*, *72*(12), 3247–3262.

Constable, C., Korte, M., & Panovska, S. (2016). Persistent high paleosecular variation activity in southern hemisphere for at least 10,000 years. *Earth and Planetary Science Letters*, *453*, 78–86.

Cox, A. (1970). Latitude dependence of the angular dispersion of the geomagnetic field. *Geophysical Journal of the Royal Astronomical Society*, *20*, 253–269.

Creer, K. (1967). *Thermal demagnetization by the continuous method*. Chapman and Hall.

Cromwell, G., Tauxe, L., Staudigel, H., & Ron, H. (2015). Paleointensity estimates from historic and modern Hawaiian lava flows using basaltic volcanic glass as a primary source material. *Physics of the Earth and Planetary Interiors*, *241*, 44–56.

Cromwell, G., Trusdell, F., Tauxe, L., Staudigel, H., & Ron, H. (2018). Holocene paleointensity of the island of Hawai'i from glassy volcanics. *Geochemistry, Geophysics, Geosystems*, *19*, 3224–3245. https://doi.org/10.1002/2017GC006927

Dodson, M., & McClelland-Brown, E. (1980). Magnetic blocking temperatures of single-domain grains during slow cooling. *Journal of Geophysical Research*, *85*, 2625–2637.

Dossing, A., Muxworthy, A., Supakulopas, R., Riishuus, M., & Mac Niocaill, C. (2016). High northern geomagnetic field behavior and new constraints on the Gilsa event: Paleomagnetic and ^{40}Ar/^{39}Ar. *Earth and Planetary Science Letters*, *456*, 98–111.

Dunlop, D., & Özdemir, O. (2001). Beyond Néel's theories: Thermal demagnetization of narrow-band partial thermoremanent magnetization. *Physics of the Earth and Planetary Interiors*, *126*, 43–57.

Dunlop, D., Zhang, B., & Özdemir, O. (2005). Linear and nonlinear Thellier paleointensity behavior of natural minerals. *Journal of Geophysical Research*, *110*, B01103. https://doi.org/10.1029/2004JB003095

Esser, R., Kyle, P., & McIntosh, W. (2004). 40Ar/39Ar dating of the eruptive history of Mount Erebus, Antarctica: Volcano evolution. *Bulletin of Volcanology*, *66*, 671–686.

Fisher, R. A. (1953). Dispersion on a sphere. *Proceedings of the Royal Society, A*, *217*, 295–305.

Fox, J., & Aitken, M. (1980). Cooling-rate dependence of thermoremanent magnetisation. *Nature*, *283*, 462–463.

Gilbert, W. (1958). *On the magnet, facsimile of 1900 translation by Silvanus P. Thompson and the Gilbert Club*. New York: Basic Books, Inc.

Glatzmaier, G., & Coe, R. (2007). Magnetic polarity reversals in the core. In Core dynamics (Vol. 5, pp. 283–297). Elsevier.

Gradstein, F., Ogg, J., Schmitz, M., & Ogg, G. (2012). *Geologic time scale 2012*. Amsterdam: Elsevier.

Halgedahl, S., & Fuller, M. (1980). Magnetic domain observations of nucleation processes in fine particles of intermediate titanomagnetite. *Nature*, *288*, 70–72.

Harrison, R., & Feinberg, J. (2008). An improved algorithm for calculating first-order reversal curve distributions using locally weighted regression smoothing. *Geochemistry, Geophysics, Geosystems*, *9*, Q05016. https://doi.org/10.1029/2008GC001987

Heaton, D., & Koppers, A. (2019). High-resolution ^{40}Ar/^{39}Ar geochronology of the Louisville Seamounts IODP Expedition 330 drill sites: Implications or the duration of hot spot-related volcanism and age progressions. *Geochemistry, Geophysics, Geosystems*, *46*, 4073–4102. https://doi.org/10.1029/2019GL083542

Hoffman, K., & Biggin, A. (2005). A rapid multi-sample approach to the determination of absolute paleointensity. *Journal of Geophysical Research*, *110*, B12108.

Holme, R. (2007). Large-scale flow in the core. In Core dynamics (Vol. 5, pp. 107–130). Elsevier.

Irving, E., Robertson, W., Stott, P., Tarling, D., & Ward, M. (1961). Treatment of partially stable sedimentary rocks showing planar distribution of directions of magnetization. *Journal of Geophysical Research*, *66*(6), 1927–1933.

Jackson, A., & Finlay, C. (2007). Geomagnetic secular variation and its applications to the core. In: *Geomagnetism* (Vol. *5*, pp. 147–193). Elsevier.

Jackson, A., Jonkers, A. R. T., & Walker, M. R. (2000). Four centuries of geomagnetic secular variation from historical records. *Philosophical Transactions Royal Society of London, Series A*, *358*(1768), 957–990.

Johnson, C. L., Constable, C. G., Tauxe, L., Barendregt, R., Brown, L., Coe, R., & Stone, D. (2008). Recent investigations of the 0–5 Ma geomagnetic field recorded in lava flows. *Geochemistry, Geophysics, Geosystems*, *9*, Q04032. https://doi.org/10.1029/2007GC001696

Juarez, T., Tauxe, L., Gee, J. S., & Pick, T. (1998). The intensity of the earth's magnetic field over the past 160 million years. *Nature*, *394*, 878–881.

Kirschvink, J. L. (1980). The least-squares line and plane and the analysis of paleomagnetic data. *Geophysical Journal of the Royal Astronomical Society*, *62*, 699–718.

Kissel, C., & Laj, C. (2004). Improvements in procedure and paleointensity selection criteria (PICRIT-03) for Thellier and Thellier determinations: Application to Hawaiian basaltic long cores. *Physics of the Earth and Planetary Interiors*, *147*, 155–169.

Koppers, A., Russell, J., Jackson, M., Konter, J., Staudigel, H., & Hart, S. (2008). Samoa reinstated as a primary hotspot trail. *Geology*, *36*, 435–438. https://doi.org/10.1130/G24630A.1

Krása, D., Heunemann, C., Leonhardt, R., & Petersen, N. (2003). Experimental procedure to detect multidomain remanence during Thellier-Thellier experiments. *Physics and Chemistry of the Earth*, *28*, 681–687. https://doi.org/10.1016/S1474-7065(03)00122-0

Lawrence, K. P., Tauxe, L., Staudigel, H., Constable, C., Koppers, A., McIntosh, W. C., & Johnson, C. L. (2009). Paleomagnetic field properties near the southern hemisphere tangent cylinder. *Geochemistry, Geophysics, Geosystems*, *10*, Q01005. https://doi.org/10.1029/2008GC00207

Leonhardt, R., Heunemann, C., & Krasa, D. (2004). Analyzing absolute paleointensity determinations: Acceptance criteria and the software ThellierTool4.0. *Geochemistry, Geophysics, Geosystems*, *5*, Q12016. https://doi.org/10.1029/2004GC000807

Livermore, P., Fournier, A., & Gallet, Y. (2014). Core-flow constraints on extreme archeomagnetic intensity changes. *Earth and Planetary Science Letters*, *387*, 145–156. https://doi.org/10.1016/j.epsl.2013.11.020

Lowes, F. (1973). Spatial power spectrum of the main geomagnetic field, and extrapolation to the core. *Geophysical Journal of the Royal Astronomical Society*, *36*, 717–730.

Mankinen, E., & Cox, A. (1988). Paleomagnetic investigation of some volcanic rocks from the McMurdo Volcanic Province, Antarctica. *Journal of Geophysical Research*, *93*(B10), 11599–11612.

McElhinny, M. (1973). *Paleomagnetism and plate tectonics*. Cambridge: Cambridge University Press.

McElhinny, M. (2007). Encyclopedia of geomagnetism and paleomagnetism. In D. Gubbins, & E. Herrero-Bervera (Eds.), *Geocentric axial dipole hypothesis)*. Springer-Verlag. https://doi.org/10.1007/978-1-4020-4423-6_107

McElhinny, M., & Lock, J. (1996). Iaga paleomagnetic databases with access. *Surveys in Geophysics*, *17*(5), 575–591.

McFadden, P., & McElhinny, M. (1982). Variations in the geomagnetic dipole 2: Statistical analysis of VDMs for the past 5 m.y. *Journal of Geomagnetism and Geoelctricity*, *34*, 163–189.

McFadden, P., Merrill, R., & McElhinny, M. (1988). Dipole-quadrupole family modeling of paleosecular variation. *Journal of Geophysical Research*, *93*, 11583–11588.

Nagata, T., Arai, Y., & Momose, K. (1963). Secular variation of the geomagnetic total force during the last 5000 years. *Journal of Geophysical Research*, *68*, 5277–5282.

Néel, L. (1955). Some theoretical aspects of rock-magnetism. *Advances in Physics*, *4*, 191–243.

Opdyke, N., & Henry, K. (1969). A test of the dipole hypothesis. *Earth and Planetary Science Letters*, *6*, 139–151.

Paterson, G. (2011). A simple test for the presence of multidomain behavior during paleointensity experiments. *Journal of Geophysical Research*, *116*, B10104.

Paterson, G., Tauxe, L., Biggin, A., Shaar, R., & Jonestrask, L. (2014). On improving the selection of Thellier-type paleointensity data. *Geochemistry, Geophysics, Geosystems*, *15*(4), 1180–1192. https://doi.org/10.1002/2013GC005135

Pike, C., Roberts, A., & Verosub, K. (1999). Characterizing interactions in fine magnetic particle systems using first order reversal curves. *Journal of Applied Physics*, *85*, 6660–6667.

Pike, C., Roberts, A., & Verosub, K. (2001). First-order reversal curve diagrams and thermal relaxation effects in magnetic particles. *Geophysical Journal International*, *145*, 721–730.

Roberts, A. P., Pike, C. R., & Verosub, K. (2000). First-order reversal curve diagrams: A new tool for characterizing the magnetic properties of natural samples. *Journal of Geophysical Research*, *106*, 28461–28475.

Santos, C., & Tauxe, L. (2019). Investigating the accuracy, precision, and cooling rate dependence of laboratory-acquired thermal remanences during paleointensity experiments. *Geochemistry, Geophysics, Geosystems*, *20*, 383–397.

Selkin, P., Gee, J., & Tauxe, L. (2007). Nonlinear thermoremanence acquisition and implications for paleointensity data. *Earth and Planetary Science Letters*, *256*, 81–89.

Selkin, P., & Tauxe, L. (2000). Long-term variations in paleointensity. *Philosophical Transactions of the Royal Society of London – A*, *358*, 1065–1088.

Shaar, R., & Tauxe, L. (2013). Thellier_GUI: An integrated tool for analyzing paleointensity data from Thellier-type experiments. *Geochemistry, Geophysics, Geosystems*, *14*, 677–692.

Shashkanov, V., & Metallova, V. (1972). Violation of Thellier's law for partial thermoremanent magnetizations. *Izvestiya, Atmospheric and Oceanic Physics*, *3*, 80–86.

Shaw, J. (1974). A new method of determining the magnitude of the paleomagnetic field application to 5 historic lavas and five archeological samples. *Geophysical Journal of the Royal Astronomical Society*, *39*, 133–141.

Smirnov, A. V., & Tarduno, J. A. (2003). Magnetic hysteresis monitoring of cretaceous submarine basaltic glass during Thellier paleointensity experiments: Evidence for alteration and attendant low field bias. *Earth and Planetary Science Letters*, *206*(3–4), 571–585.

Stephenson, A. (1967). *Apparatus for the thermal demagnetization by the progressive method*. Chapman and Hall.

Tanaka, H., & Kobayashi, T. (2003). Paleomagnetism of the late quaternary Ontake volcano, Japan: Directions, intensities, and excursions. *Earth Planets and Space*, *55*(4), 189–202.

Tanaka, H., Kono, M., & Uchimura, H. (1995). Some global features of paleointensity in geological time. *Geophysical Journal International*, *120*, 97–102.

Tauxe, L., Kylstra, N., & Constable, C. (1991). Bootstrap statistics for paleomagnetic data. *Journal of Geophysical Research*, *96*, 11723–11740.

Tauxe, L., Gans, P., & Mankinen, E. (2004). Paleomagnetism and ^{40}Ar/^{39}Ar ages from volcanics extruded during the Matuyama and Brunhes chrons near McMurdo sound, Antarctica. *Geochemistry, Geophysics, Geosystems*, *5*(6).

Tauxe, L., Gee, J., Steiner, M., & Staudigel, H. (2013). Paleointensity results from the Jurassic: New constraints from submarine basaltic glasses of ODP Site 801C. *Geochemistry, Geophysics, Geosystems*, *14*(10), 4718–4733. https://doi.org/10.1002/ggge/20282

Tauxe, L., & Kent, D. V. (2004). A simplified statistical model for the geomagnetic field and the detection of shallow bias in paleomagnetic inclinations: Was the ancient magnetic field dipolar? In J. E. T. Channell (Ed.), Timescales of the paleomagnetic field. (Vol. *145*, pp. 101–116). Washington, DC: American Geophysical Union. https://doi.org/10.1029/145GM08

Tauxe, L., Shaar, R., Jonestrask, L., Swanson-Hysell, N., Minnett, R., Koppers, A. A. P., &, Fairchild, L. (2016). PmagPy: Software package for paleomagnetic data analysis and a bridge to the Magnetics Information Consortium (MagIC) database. *Geochemistry, Geophysics, Geosystems*, *17*, 2450–2463. https://doi.org/10.1002/2016GC006307

Tauxe, L., & Staudigel, H. (2004). Strength of the geomagnetic field in the cretaceous normal superchron: New data from submarine basaltic glass of the troodos ophiolite. *Geochemistry, Geophysics, Geosystems*, *5*(2), Q02H06. https://doi.org/10.1029/2003GC000635

Tauxe, L., & Yamazaki, T. (2015). Paleointensities. In M. Kono (Ed.), Geomagnetism.(Vol. *5*, 2nd ed., pp. 461–509). Elsevier.

Thébault, E., Finlay, C., Beggan, C., Alken, P., Aubert, J., Barrois, O., &, Lowes, F. (2015). International Geomagnetic Reference Field: The 12th generation. *Earth Planets and Space*, *67*, 67–79. https://doi.org/10.1186/s40623-015-0228-9

Thellier, E. (1938). Sur l'aimantation des terres cuites et ses applications géophysique. *Annales de l'institut de physique du globe de l'Université de Paris*, *16*, 157–302.

Thellier, E., & Thellier, O. (1959). Sur l'intensité du champ magnétique terrestre dans le passé historique et géologique. *Annals of Geophysics*, *15*, 285–378.

Vandamme, D. (1994). A new method to determine paleosecular variation. *Physics of the Earth and Planetary Interiors*, *85*, 131–142.

Walton, D., & Shaw, J. (1992). Microwave demagnetization. *Journal of Applied Physics*, *71*, 1549.

Wang, H., Kent, D., & Rochette, P. (2015). Weaker axially dipolar time-averaged paleomagnetic field based on multidomain-corrected paleointensities from Galapagos lavas. *Proceedings of the National Academy of Sciences of the United States of America*, *112*, 15036–15041. https://doi.org/10.1073/pnas.1505450112

Watkins, N. (1973). Brunhes epoch geomagnetic secular variation on Reunion Island. *Journal of Geophysical Research*, *78*(32), 7763–7768.

Wilch, T., Lux, D., Denton, G., & McIntosh, W. (1993). Minimal pliocene-pleistocene uplift of the dry valleys sector of the transarctic mountains: A key parameter in ice-sheet reconstructions. *Geology*, *21*, 841–844.

Yu, Y., Tauxe, L., & Genevey, A. (2004). Toward an optimal geomagnetic field intensity determination technique. *Geochemistry, Geophysics, Geosystems*, *5*, Q02H07. https://doi.org/10.1029/2003GC000630

Ziegler, L., Constable, C., Johnson, C. L., & Tauxe, L. (2011). PADM2M: A penalized maximum likelihood model of the 0-2 Ma paleomagnetic axial dipole moment. *Geophysical Journal International*, *184*, 1069–1089.

Zijderveld, J. D. A. (1967). *A.C. Demagnetization of rocks: Analysis of results*. Chapman and Hall.